The Astrophysical Journal, 812:28 (18pp), 2015 October 10 doi:10.1088/0004-637X/812/1/28

POLARIZED LINE FORMATION IN MOVING ATMOSPHERES WITH PARTIAL FREQUENCY REDISTRIBUTION AND A WEAK MAGNETIC FIELD

M. Sampoorna and K. N. Nagendra
Indian Institute of Astrophysics, Koramangala, Bengaluru 560 034, India; sampoorna@iiap.res.in, knn@iiap.res.in
Received 2015 April 20; accepted 2015 September 3; published 2015 October 6

ABSTRACT

The dynamical state of the solar and stellar atmospheres depends on the macroscopic velocity fields prevailing within them. The presence of such velocity fields in the line formation regions strongly affects the polarized radiation field emerging from these atmospheres. Thus it becomes necessary to solve the radiative transfer equation for polarized lines in moving atmospheres. Solutions based on the "observer's frame method" are computationally expensive to obtain, especially when partial frequency redistribution (PRD) in line scattering and large-amplitude velocity fields are taken into account. In this paper we present an efficient alternative method of solution, namely, the comoving frame technique, to solve the polarized PRD line formation problems in the presence of velocity fields. We consider one-dimensional planar isothermal atmospheres with vertical velocity fields. We present a study of the effect of velocity fields on the emergent linear polarization profiles formed in optically thick moving atmospheres. We show that the comoving frame method is far superior when compared to the observer's frame method in terms of the computational speed and memory requirements.

Key words: line: profiles – polarization – radiative transfer – scattering – stars: atmospheres – Sun: chromosphere

1. INTRODUCTION

The atmospheres of hot stars with fast stellar winds (like those in O stars or Wolf–Rayet stars), expanding nebulae, novae, supernovae, quasars, and rapidly changing solar prominences are some of the examples for which fluid motions cannot be neglected when calculating the polarized radiation field emerging from them. This is because the velocity gradients present in the regions of spectral line formation significantly affect the linear polarization profiles by producing Doppler-shifted asymmetric line profiles and considerably modifying the polarization amplitudes compared to the static case (see, e.g., Nagendra 1996; Carlin et al. 2012). The solution of the polarized radiative transfer equation in moving atmospheres is considerably more complicated than its static counterpart. This is because in a moving atmosphere the projected velocity keeps changing as the ray traverses through the medium, thereby complicating the angle, frequency, and spatial coupling of different rays. The complexity of the problem escalates when partial frequency redistribution (PRD) in line scattering is taken into account, because of the inherent coupling between angles and frequencies. Thus most of the studies on the effects of velocity fields on polarization profiles of spectral lines are limited to the approximation of complete frequency redistribution (CRD) in line scattering (see, e.g., Sengupta 1993; Hillier 1994, 1996; Carlin et al. 2012, 2013; Milić & Faurobert 2014; Carlin & Asensio Ramos 2015). One of the early papers where the polarized PRD line transfer in moving atmospheres is studied is that by Nagendra (1996). Recently the same problem in the presence of a weak magnetic field was considered by Sampoorna & Nagendra (2015).

The polarized radiative transfer equation with velocity fields can be solved in the observer's frame or in the comoving frame. The observer's frame method is numerically expensive and is suitable only for low-velocity fields, because in this method the Doppler shifts introduced by the velocity field are dealt with directly. As a result the inextricable coupling between the angle, frequency, and spatial points needs to be treated numerically, requiring the use of large frequency bandwidth and fine distribution of angle and spatial grid points. On the other hand, the comoving frame method is the method of choice as it can handle both low- and high-velocity fields. Further, since the observer moves along with the fluid, the relative velocity shift between the fluid and the observer is zero, allowing the use of frequency, angle and spatial quadratures, which are good enough for the corresponding static atmosphere. For a detailed discussion of these two methods for unpolarized line transfer in moving atmospheres the reader is referred to Mihalas (1978, see also Hubeny & Mihalas 2014).

In Sampoorna & Nagendra (2015) the polarized radiative transfer equation with velocity fields, PRD, and magnetic fields was solved in the observer's frame. As already mentioned above, in the observer's frame method we need to consider large frequency bandwidths (because of Doppler shifts), a fine angle grid (to account for strong angle–frequency coupling), and a fine spatial grid (to accurately compute the optical depth increments in the formal solution). Furthermore, when the PRD mechanism is included, which has its own angle–frequency couplings, the accurate evaluation of the PRD line source vector (that contains the scattering integral) becomes computationally expensive. The linear polarization, being a sensitive quantity, also demands higher resolution in angle and frequency variables, thereby increasing the dimensionality of the problem. Thus the polarized line radiative transfer in the observer's frame becomes computationally very expensive even for low-velocity fields. For these reasons, only a few studies with optically thin slabs were presented in Sampoorna & Nagendra (2015).

In the present paper we develop the comoving frame method for solving polarized radiative transfer in moving atmospheres. To this end we extend the method of Baron & Hauschildt (2004, hereafter BH04) developed for the unpolarized transfer in spherical media, to the case of polarized transfer in planar media. BH04 solve the comoving frame unpolarized radiative transfer equation in spherical media with non-monotonic

velocity fields using accelerated lambda iteration (ALI). The ALI methods are based on the concept of operator splitting or operator perturbation (see Cannon 1973). Based on this concept different approximate lambda operators (such as diagonal, tri-diagonal, penta-diagonal etc.) have been employed to accelerate the convergence of the ALI method (see the review by Hubeny 2003, for details). BH04 used a tri-diagonal approximate lambda operator and a short-characteristic formal solver. Unlike BH04, here we use a diagonal approximate lambda operator and also limit our attention to monotonic velocity fields. We consider three cases of frequency redistribution mechanism in line scattering, namely the approximation of CRD, angle-averaged PRD, and angle-dependent PRD. In the case of CRD and angle-averaged PRD we develop a comoving frame polarized ALI method, while for the angle-dependent PRD we develop a comoving frame scattering expansion method (SEM; see, e.g., Nagendra & Sampoorna 2011). The comoving frame methods developed here are numerically efficient and sufficiently robust to study the effect of velocity fields on optically thick polarized spectral lines.

The velocity and magnetic fields are both present in the solar atmosphere. However, we have assumed in this paper that the flows do not affect the magnetic fields and vice versa. Magnetic fields affect the line profiles through the Hanle effect, whereas velocity fields do so through the Doppler effects they cause in the absorption and emission profiles. Such an assumption is valid when the fields are weak and the flows do not alter the equilibrium structure of the atmosphere significantly (low-velocity regime). It is important to learn the impact of flows in the low-velocity regime on the polarization signals arising due to the Hanle effect. Since a realistic study of the problem produces profiles that cannot easily be interpreted, as a first step, we work with known vector magnetic fields and known velocity fields through an empirical study. It is shown that the neglect of velocity fields causes a considerable effect on the Hanle diagnostics. This is because the vertical velocity gradients significantly modify the linear polarization amplitudes and shapes compared to the static case (see Carlin et al. 2012; Sampoorna & Nagendra 2015, and Section 4 of the present paper) and thereby should be accounted for to correctly reproduce the observed linear polarization profiles and to correctly infer the magnetic field.

In Section 2 we present the polarized PRD transfer equation in both the observer's and comoving frames. The numerical methods of solution to solve these equations are presented in Section 3, where we also discuss the convergence properties of the comoving frame methods. Numerical results are presented in Section 4 and conclusions in Section 5. The computational requirements of the comoving frame as well as observer's frame method are discussed in the appendix.

2. POLARIZED TRANSFER EQUATION

We consider a one-dimensional planar isothermal atmosphere with velocity fields along the atmospheric normal, and a two-level atom model with an infinitely sharp and unpolarized lower level. In an optically thick absorbing and scattering medium, it is necessary to self-consistently solve the polarized transfer equation and the statistical equilibrium equation to obtain a correct solution. For a two-level atom the statistical equilibrium equation takes the form of a line source vector. In Section 2.1, we first recall the observer's frame transfer equation both in the Stokes representation (see Section 2.1.1) and in the so-called irreducible basis (see Sections 2.1.2 and 2.1.3). The observer's frame irreducible transfer equation is then transformed to the comoving frame in Section 2.2.

2.1. Observer's Frame

For the sake of clarity, here we recall the polarized transfer equation in the observer's frame.

2.1.1. Stokes Representation

In the Stokes representation the polarized radiation field is characterized by the four Stokes parameters I, Q, U, and V, with I denoting the specific intensity, Q and U the degree and plane of linear polarization, and V the circular polarization. In the presence of a weak magnetic field $\boldsymbol{B}$, the Stokes V gets decoupled from (I, Q, U) and is not generated by the weak-field Hanle effect unless circularly polarized radiation is given as an input. Thus Stokes $V = 0$ for the problem at hand. Therefore we define the 3-component Stokes vector $\boldsymbol{I} = (I, Q, U)^{\mathrm{T}}$. Further, we define the reference direction for positive Stokes Q to be perpendicular to the nearest limb. The Stokes transfer equation in the observer's frame is given by

$$\mu \frac{\partial \boldsymbol{I}(\tau, x, \boldsymbol{\Omega})}{\partial \tau} = \boldsymbol{I}(\tau, x, \boldsymbol{\Omega}) - \boldsymbol{S}(\tau, x, \boldsymbol{\Omega}), \quad (1)$$

where $\boldsymbol{\Omega}(\theta, \phi)$ is the ray direction with respect to the atmospheric normal, and $\mu = \cos\theta$. The monochromatic optical depth is given by $d\tau = [\varphi(x, \mu) + r]d\tau_l$, with $d\tau_l$ being the line-integrated optical depth. The normalized Voigt function $\varphi(x, \mu) = H(a, x - \mu V)$, where a is the damping parameter, $x = (\nu - \nu_0)/\Delta\nu_{\mathrm{D}}$ (with ν_0 being the line center frequency and $\Delta\nu_{\mathrm{D}}$ the Doppler width) and V is a non-dimensional velocity defined as $V = (\nu_0/c)v_z/\Delta\nu_{\mathrm{D}}$ (with v_z being the vertical velocity field). The ratio of the continuum to line absorption coefficient is denoted by r. The total source vector is given by

$$\boldsymbol{S}(\tau, x, \boldsymbol{\Omega}) = \frac{\varphi(x, \mu)\boldsymbol{S}_l(\tau, x, \boldsymbol{\Omega}) + r\boldsymbol{S}_c}{\varphi(x, \mu) + r}, \quad (2)$$

where the unpolarized continuum source vector is given by $\boldsymbol{S}_c = B_{\nu_0}\boldsymbol{U}$, with B_{ν_0} the Planck function at the line center and $\boldsymbol{U} = (1, 0, 0)^{\mathrm{T}}$. For a two-level atom with infinitely sharp and unpolarized lower level, the line source vector has the form

$$\boldsymbol{S}_l(\tau, x, \boldsymbol{\Omega}) = \epsilon B_{\nu_0}\boldsymbol{U} + \int_{-\infty}^{+\infty} dx' \frac{1}{4\pi} \oint \sin\theta' d\theta' \times d\phi' \frac{\boldsymbol{R}\left(x, \boldsymbol{\Omega}, x', \boldsymbol{\Omega}', \boldsymbol{B}\right)}{\varphi(x, \mu)} \boldsymbol{I}\left(\tau, x', \boldsymbol{\Omega}'\right), \quad (3)$$

where $\boldsymbol{\Omega}'(\theta', \phi')$ is the incident ray direction with respect to the atmospheric normal, and ϵ is the thermalization parameter. The exact form of the Hanle redistribution matrix $\boldsymbol{R}$ is given by Approximation I of Bommier (1997). The explicit expressions for both the angle-dependent and angle-averaged versions of this matrix can be found in Nagendra & Sampoorna (2011, see also Sampoorna 2014) and Sampoorna et al. (2008) respectively. In the limit of CRD the matrix $\boldsymbol{R} = \varphi(x, \mu)\varphi(x', \mu')\boldsymbol{P}_{\mathrm{H}}(\boldsymbol{\Omega}, \boldsymbol{\Omega}', \boldsymbol{B})$, where the

explicit form of the Hanle phase matrix $\boldsymbol{P}_{\rm H}$ is given in Stenflo (1994, see also Landi Degl'Innocenti & Landolfi 2004).

The source vector describes the interaction of the radiation field with the medium as it traverses through the atmosphere. Under local thermodynamic equilibrium (LTE), the source vector is given by the Planck function, which is determined exclusively by the local temperature. However, in a scattering-dominated atmosphere, the non-local coupling of the atmosphere over distances that are of the order of the photon mean free path becomes important. This non-local coupling is contained in the expression for the line source vector through the scattering integral (see Equation (3)). Clearly the source vector becomes decoupled from the local temperature and instead is determined by the radiation field from non-local sources. Therefore, unlike LTE where a ray-by-ray solution is feasible, in non-LTE different rays are coupled in direction, frequency, and space, thereby making the method of solution considerably complex. Further, the LTE transfer equation is an ordinary differential equation while the non-LTE transfer equation is an integro-differential equation. Therefore Equations (1)–(3) form a system of coupled equations, which along with the boundary conditions define the so-called non-LTE problem of the first kind when polarization is neglected and of the second kind when it is included (see Landi Degl'Innocenti & Landolfi 2004). One needs to determine the source vector and the radiation field consistently with one another. In other words, the source vector at each depth point is determined by the local radiation field, which itself is determined by the source vector at all other depth points in the medium. In a moving atmosphere, the complexity of the non-LTE problem of the second kind is further enhanced. This is because, due to scattering, the projected velocities keep changing as the ray traverses through the medium, thereby further complicating the angle, frequency, and spatial coupling of different rays. Therefore the numerical methods developed for a static atmosphere cannot easily be adapted to the moving atmosphere, especially for rapidly varying arbitrary velocity fields.

2.1.2. Irreducible Basis for Angle-averaged PRD

For a static atmosphere, Frisch (2007, see also Nagendra et al. 1998) has shown that it is possible to decompose the Stokes vector $\boldsymbol{I}$ and the source vector $\boldsymbol{S}$ into six irreducible components. When CRD or angle-averaged PRD is chosen as the frequency redistribution mechanism, these irreducible components are cylindrically symmetric. Numerical methods developed based on these cylindrically symmetric components are far superior to those developed using Stokes vectors, which are inherently non-axisymmetric. Hence it is advantageous to work in an irreducible basis.

This decomposition technique of Frisch (2007) can also be applied to the case of moving atmospheres. Thus the Stokes vector $\boldsymbol{I}$ and the line source vector $\boldsymbol{S}_l$ can be decomposed as

$$I_i(\tau, x, \boldsymbol{\Omega}) = \sum_{K=0,2} \sum_{Q=-K}^{Q=+K} \mathcal{T}^K_Q(i, \boldsymbol{\Omega}) I^K_Q(\tau, x, \mu), \tag{4}$$

$$S_{i,l}(\tau, x, \boldsymbol{\Omega}) = \sum_{K=0,2} \sum_{Q=-K}^{Q=+K} \mathcal{T}^K_Q(i, \boldsymbol{\Omega}) S^K_{l,Q}(\tau, x, \mu), \tag{5}$$

where $i = 0, 1, 2$ denote the Stokes parameters I, Q, and U. In the above expressions $\mathcal{T}^K_Q(i, \boldsymbol{\Omega})$ are the irreducible tensors for polarimetry (see Landi Degl'Innocenti & Landolfi 2004), with K being the multipolar index taking values 0 and 2, and $Q \in [-K, +K]$.

In the case of a static atmosphere, the irreducible components of the line source vector $S^K_{l,Q}$ become independent of both θ and ϕ. In a moving atmosphere $S^K_{l,Q}$ corresponding to the case of CRD retains this angle-independence. However, in the case of angle-averaged PRD $S^K_{l,Q}$ becomes independent only of the azimuth ϕ. This is because the angle-averaged redistribution function now depends on μ and μ', as we need to replace x and x' by the corresponding Doppler-shifted frequencies, namely, $x - \mu V$ and $x' - \mu' V$ respectively. Unlike in CRD, the incoming and outgoing frequencies are coupled in PRD. Thus the presence of velocity fields brings in an additional coupling between the incoming (μ') and outgoing (μ) angles. As a result $S^K_{l,Q}$ for angle-averaged PRD is no longer independent of μ in contrast to the static case. Because of the angle (μ) dependence of the absorption profile function, the irreducible components of the total source vector (S^K_Q) for both CRD and angle-averaged PRD explicitly depend on μ, unlike the static case. In this way the case of a moving atmosphere is characteristically different from that of the static case.

We define the real irreducible components as $I^{xK}_Q = \Re(I^K_Q)$ and $I^{yK}_Q = \Im(I^K_Q)$. In matrix notation, the transfer equation for the real irreducible components may be written as

$$\mu \frac{\partial \boldsymbol{\mathcal{I}}(\tau, x, \mu)}{\partial \tau} = \boldsymbol{\mathcal{I}}(\tau, x, \mu) - \boldsymbol{\mathcal{S}}(\tau, x, \mu), \tag{6}$$

where $\boldsymbol{\mathcal{I}} = \left(I^0_0, I^2_0, I^{x2}_1, I^{y2}_1, I^{x2}_2, I^{y2}_2\right)^{\rm T}$. The irreducible source vector $\boldsymbol{\mathcal{S}}$ has a form similar to Equation (2), but with the irreducible line source vector now given by

$$\boldsymbol{\mathcal{S}}_l(\tau, x, \mu) = \boldsymbol{\mathcal{G}}(\tau) + \int_{-\infty}^{+\infty} dx' \frac{1}{2} \int_{-1}^{+1} d\mu' \times \frac{\boldsymbol{N}^r\left(x, \mu, x', \mu', \boldsymbol{B}\right)}{\varphi(x, \mu)} \boldsymbol{\Psi}\left(\mu'\right) \boldsymbol{\mathcal{I}}\left(\tau, x', \mu'\right), \tag{7}$$

where $\boldsymbol{\mathcal{G}}(\tau) = (\epsilon B_{\nu_0}, 0, 0, 0, 0, 0)^{\rm T}$ is the primary source vector. The explicit form of the 6×6 Hanle PRD matrix $\boldsymbol{N}^r(x, \mu, x', \mu', \boldsymbol{B})$ in the irreducible basis is given in Appendix A of Sampoorna et al. (2008), where Doppler-shifted frequencies $x - \mu V$ and $x' - \mu' V$ should be used in the redistribution functions in place of x and x'. In the case of CRD, $\boldsymbol{N}^r(x, \mu, x', \mu', \boldsymbol{B}) = \varphi(x, \mu)\varphi(x', \mu')\boldsymbol{N}^r(\boldsymbol{B})$, where the explicit form of $\boldsymbol{N}^r(\boldsymbol{B})$ can be found in Frisch (2007). As a result the $\boldsymbol{\mathcal{S}}_l$ for CRD becomes independent of both frequency x and angle μ even in the case of moving atmosphere. The elements of the 6×6 Rayleigh phase matrix $\boldsymbol{\Psi}(\mu)$ in the irreducible basis are given in Frisch (2007).

2.1.3. Irreducible Basis for Angle-dependent PRD

In the case of angle-dependent PRD, I^K_Q and S^K_Q are non-axisymmetric because the corresponding magnetic kernel $N^K_{QQ'}$ depends on the scattering angle (Θ) between the incident and scattered rays through the angle-dependent PRD functions. For the static case, Frisch (2009) has shown that the cylindrical symmetry can be recovered by Fourier-expanding the angle-dependent PRD function over the azimuth angle difference ($\phi - \phi'$). The same decomposition technique can also be applied to the present context of moving atmospheres.

Using the Fourier azimuthal expansion of the angle-dependent PRD function, it is possible to show that I_Q^K can be expanded over the azimuth ϕ as (Frisch 2009, see also Nagendra & Sampoorna 2011; Sampoorna 2014)

$$I_Q^K(\tau, x, \mathbf{\Omega}) = \frac{1}{2}\sum_{k=-\infty}^{k=+\infty} \tilde{I}_Q^{(k)K}(\tau, x, \theta)\exp[ik\phi], \quad (8)$$

with a similar expansion for S_Q^K. The Fourier coefficients $\tilde{I}_Q^{(k)K}$ satisfy a transfer equation similar to Equation (1), with the source term given by Equation (2), but with $\tilde{S}_Q^{(k)K}$, $\tilde{S}_{l,Q}^{(k)K}$, and $\tilde{S}_{c,Q}^{(k)K}$ instead of $\boldsymbol{S}$, $\boldsymbol{S}_l$, and $\boldsymbol{S}_c$ respectively. Here $\tilde{S}_{c,Q}^{(k)K} = 2\delta_{0k}\delta_{0\,K}\delta_{0Q}B_{\nu_0}$. The Fourier coefficients of the line source vector are given by

$$\tilde{S}_{l,Q}^{(k)K}(\tau, x, \theta) = \tilde{G}_Q^{(k)K}(\tau) + \int_{-\infty}^{+\infty} dx' \frac{1}{2}\int_0^{\pi} \times \sin\theta' d\theta' \sum_{Q'} \frac{\tilde{\mathcal{N}}_{QQ'}^{(k)K}\left(x, \theta, x', \theta', \boldsymbol{B}\right)}{\varphi(x, \mu)} \times \sum_{K'Q''} \frac{1}{2}\tilde{\Gamma}_{KQ',K'Q''}^{(k-k')}(\theta')\tilde{I}_{Q''}^{(k')K'}(\tau, x', \theta'), \quad (9)$$

where $\tilde{G}_Q^{(k)K}(\tau) = 2\delta_{0k}\delta_{0\,K}\delta_{0Q}\epsilon B_{\nu_0}$, and $k' = k + Q' - Q''$. Thus, for a given value of k, the values of k' get restricted to $k - 4 \leqslant k' \leqslant k + 4$. The explicit form of the azimuthal Fourier coefficients of the magnetic kernel, namely, $\tilde{\mathcal{N}}_{QQ'}^{(k)K}$, and the Fourier coefficients $\tilde{\Gamma}_{KQ',K'Q''}^{(k-k')}$ can be found in Nagendra & Sampoorna (2011, see also Sampoorna 2014). We recall that, as in the angle-averaged case, x and x' appearing in the Fourier azimuthal coefficients of the angle-dependent PRD function should be replaced by $x - \mu V$ and $x' - \mu' V$ respectively for the case of moving media.

2.2. Co-moving Frame

The observer's frame transfer equation for the irreducible components of the Stokes vector (namely, $\boldsymbol{\mathcal{I}}$ for the case of CRD and angle-averaged PRD, and $\tilde{I}_Q^{(k)K}$ for the case of angle-dependent PRD) can be transformed to the comoving frame as described in Mihalas (1978) for the unpolarized case. For simplicity, here we give the comoving frame transfer equation for the case of angle-averaged PRD. The corresponding equation for the angle-dependent PRD can be written by analogy.

For brevity, we use the same notations for different quantities in the observer's as well as the comoving frames. The comoving frame transfer equation for the irreducible intensity vector $\boldsymbol{\mathcal{I}}$ can be written as

$$\mu\frac{\partial \boldsymbol{\mathcal{I}}(\tau, x, \mu)}{\partial \tau} = \boldsymbol{\mathcal{I}}(\tau, x, \mu) - \boldsymbol{\mathcal{S}}(\tau, x) + \mu^2 \frac{dV}{d\tau}\frac{\partial \boldsymbol{\mathcal{I}}(\tau, x, \mu)}{\partial x}, \quad (10)$$

where the monochromatic optical depth in the comoving frame is given by $d\tau = [\varphi(x) + r]d\tau_l$, with the absorption profile function $\varphi(x) = H(a, x)$ which is now angle-independent. The irreducible total and the line source vectors have the same form as their observer's frame counterparts, but the profile function and the Hanle PRD matrix $\boldsymbol{N}^r$ now depend respectively on x and $(x, x', \boldsymbol{B})$ only. Therefore $\boldsymbol{\mathcal{S}}$ and $\boldsymbol{\mathcal{S}}_l$ depend only on frequency x like their static counterparts. In the case of angle-dependent PRD the azimuthal Fourier coefficients of the irreducible source vector continue to depend on θ even in the comoving frame, because of the angle dependence of the PRD function.

3. NUMERICAL METHODS

In this section we first recall the observer's frame method (Section 3.1) and then present the comoving frame method (Section 3.2).

3.1. Observer's Frame Method

Observer's frame method involves solving the transfer equation in a frame fixed to the observer. Here the relative velocities are treated through the Doppler shift formula. The method simply involves changing the frequencies x and x' to their corresponding Doppler-shifted frequencies, and computing the solution on the original frequency grid.

For a static atmosphere, the polarized accelerated lambda iteration (PALI) techniques to solve the polarized Hanle line transfer equation are developed in Nagendra et al. (1998) for CRD and in Sampoorna et al. (2008) for angle-averaged PRD (given by the so-called Approximation Ia). These numerical methods can be generalized to take into account the effects of a vertical velocity field in the observer's frame in a straightforward manner as mentioned above. In the case of CRD no additional changes appear in the PALI method, as the corresponding irreducible line source vector continues to be independent of x and μ exactly as in the static case. However, in the case of angle-averaged PRD, because of the μ dependence of the $\boldsymbol{\mathcal{S}}_l$ that still persists, the corresponding PALI method is computationally more intensive than that of the static case. To make this point clearer, we briefly present below the PALI method in the observer's frame.

For notational simplicity, we neglect the explicit dependence of $\boldsymbol{\mathcal{I}}$ and $\boldsymbol{\mathcal{S}}$ on τ. The dependences on x and μ appear as subscripts. The formal solution of Equation (6) can be written as

$$\boldsymbol{\mathcal{I}}_{x\mu} = \boldsymbol{\Lambda}_{x\mu}[\boldsymbol{\mathcal{S}}_{x\mu}] + \boldsymbol{T}_{x\mu}, \quad (11)$$

where $\boldsymbol{T}_{x\mu}$ is the directly transmitted part of the intensity vector and $\boldsymbol{\Lambda}_{x\mu}$ is the frequency- and angle-dependent (6×6) integral operator. The iteration method is based on the introduction of an approximate operator $\boldsymbol{\Lambda}^*_{x\mu}$, which is chosen to be diagonal. At each step in the iterative process, one has current estimates of $\boldsymbol{\mathcal{S}}^{(n)}_{x\mu}$ and $\boldsymbol{\mathcal{S}}^{(n)}_{l,x\mu}$, where the superscript (n) represents the nth iteration step. The line source vector corrections $\delta\boldsymbol{\mathcal{S}}^{(n)}_{l,x\mu}$ are given at each depth point by a system of linear equations:

$$\boldsymbol{A}\delta\boldsymbol{\mathcal{S}}_l^{(n)} = \boldsymbol{r}^{(n)}. \quad (12)$$

At each depth point, $\delta\boldsymbol{\mathcal{S}}_l^{(n)}$ and $\boldsymbol{r}^{(n)}$ are vectors of length $6N_x\ 2N_\mu$. Here N_x and N_μ are the numbers of frequency and angle points in the range $[-x_{\max}, +x_{\max}]$ and $[0 < \mu \leqslant 1]$ respectively. Note that unlike the static case, wherein the frequency grid in the range $[0, x_{\max}]$ would be sufficient, in the case of moving atmospheres the full frequency range is essential. The residual vector $\boldsymbol{r}^{(n)}$ measures the difference

between the current estimate $\mathcal{S}^{(n)}_{l,x\mu}$ and a formal line source vector $\mathcal{S}^{(n)}_{\mathrm{FS},l,x\mu}$ given by Equation (7) where $\mathcal{I}(\tau, x, \mu)$ is replaced by $\mathcal{I}^{(n)}_{x\mu} = \Lambda_{x\mu}\left[\mathcal{S}^{(n)}_{x\mu}\right]$. A short-characteristic formal solver is used to compute $\mathcal{I}^{(n)}_{x\mu}$.

At each depth point, the matrix $\boldsymbol{A}$ has dimensions $(6N_x\ 2N_\mu \times 6N_x\ 2N_\mu)$ in contrast to the static case where it had the dimension of $(6[N_x/2] \times 6[N_x/2])$. For a given x, x', μ, and μ', the matrix $\boldsymbol{A}$ can be decomposed into $(N_x\ 2N_\mu \times N_x\ 2N_\mu)$ blocks of 6×6 elements. In each block, denoted by $\boldsymbol{\mathcal{A}}$, the elements may be written as

$$\boldsymbol{\mathcal{A}} = \delta_{mn}\,\delta_{\alpha\beta}\,\boldsymbol{E} - w_\beta\,\bar{w}_n\,p_{n\beta}\,\frac{\boldsymbol{N}^r_{m\alpha,n\beta}}{\varphi_{m\alpha}}\,\boldsymbol{\Psi}_\beta\,\boldsymbol{\Lambda}^*_{n\beta}, \qquad (13)$$

where $m = 1, \cdots, N_x$, $n = 1, \cdots, N_{x'}$, $\alpha = 1, \cdots, 2N_\mu$, and $\beta = 1, \cdots, 2N_{\mu'}$, and $\boldsymbol{E}$ is the identity operator. The coefficients w_β and $\bar{w}_n$ denote the μ' and x' integration weights. In Equation (13) $p_{n\beta} = \varphi_{n\beta}/(\varphi_{n\beta} + r)$ and δ_{mn} is the Kronecker symbol. The matrix $\boldsymbol{A}$ is computed only once as it does not change during the iteration. This method of computing the line source vector corrections is referred to as the frequency-angle by frequency-angle method (Sampoorna et al. 2011), and is a generalization of the frequency by frequency method of Paletou & Auer (1995) to the present problem.

For the case of the polarized Hanle line transfer equation with angle-dependent PRD (given by the Approximation I of Bommier 1997) in static media, a SEM has been developed in Nagendra & Sampoorna (2011). This method can be generalized to the case of moving atmospheres in the observer's frame in a straightforward manner. Hence we do not present the steps of this method again. For a review on PALI and SEM techniques for PRD problems, the reader is referred to Nagendra & Sampoorna (2009) and Nagendra (2014). The computational requirements of the observer's frame method discussed in this section are presented in Appendix A.1.

3.2. Co-moving Frame Method

The comoving frame method involves solving the transfer equation in a frame fixed to the fluid and then transforming the solution obtained to the observer's frame. Thus the actual computation consists of two steps: in the first step, the comoving frame transfer equation is solved iteratively (either using a PALI method or SEM) to obtain the converged comoving frame polarized source and the Stokes vectors in the irreducible basis. In the second step, a formal integration of the transfer equation is performed in the observer's frame in order to obtain the observer's frame emergent polarized radiation field still in the irreducible basis. This step involves transforming the comoving frame solution obtained on the comoving frame frequency grid onto the observer's frame frequency grid. Basically we need to interpolate the comoving frame source vector $\boldsymbol{S}$ onto the observer's frame frequency grid, which is related to the comoving frame frequency grid through Doppler shifts (see Nagendra 1996 for more details). Finally the observer's frame irreducible emergent Stokes vector is transformed to the Stokes representation using a simple transformation formula (see Frisch 2007).

The comoving frame transfer equation differs from that of the static case only by an extra term called the comoving frame term (see Equation (10)). As a result the basic steps of the PALI method as well as the SEM in the comoving frame remain the same as in the corresponding static case. Therefore we do not repeat those steps here. The main difference between the static case and the comoving frame solution method is in the formal solution and the construction of the approximate Λ-operator (chosen here to be diagonal). In the following subsections we discuss them in more detail. We discuss the computational requirements of the comoving frame method in Appendix A.2.

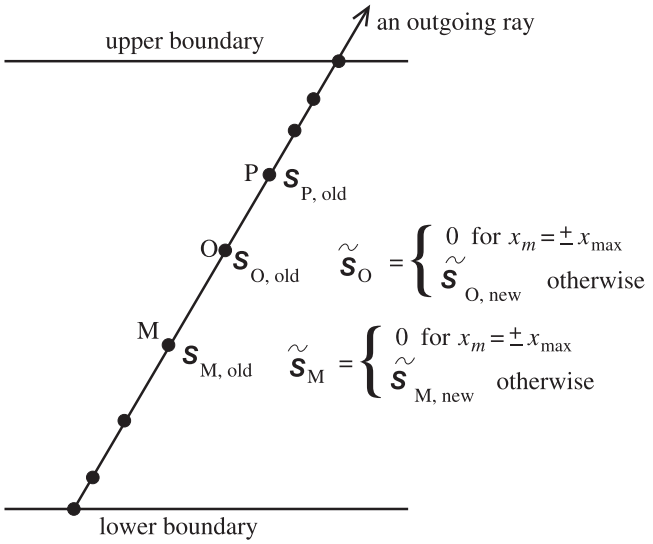

Figure 1. Schematic representation of the one-dimensional short-characteristic formal solution on an MOP stencil for an outgoing ray in a moving atmosphere. "Old" denotes the previous iterate values and "new" denotes the values of $\tilde{\boldsymbol{S}}$ that are calculated using the intensity for the previous frequency point (see Equations (18)–(20)) that has been computed in the current iterate formal solution. A similar formal solution method is applied to the incoming ray as well.

3.2.1. Formal Solution

As in Section 2.2, here we present the formal solution for the case of angle-averaged PRD. It is straightforward to extend the equations presented here to the case of angle-dependent PRD. Following BH04, we define

$$\tilde{\boldsymbol{\mathcal{S}}}(\tau, x, \mu) = -\mu^2\,\frac{dV}{d\tau}\,\frac{\partial \boldsymbol{\mathcal{I}}(\tau, x, \mu)}{\partial x}. \qquad (14)$$

We also define the total monochromatic optical depth along the ray as $d\tau^{\mathrm{tot}} = d\tau/\mu$. For brevity of notation we will here call $d\tau^{\mathrm{tot}}$ as $d\tau$ itself. Thus, Equation (10) can be rewritten as

$$\frac{\partial \boldsymbol{\mathcal{I}}(\tau, x, \mu)}{\partial \tau} = \boldsymbol{\mathcal{I}}(\tau, x, \mu) - \boldsymbol{\mathcal{S}}(\tau, x) - \tilde{\boldsymbol{\mathcal{S}}}(\tau, x, \mu). \qquad (15)$$

We follow the short-characteristic integration technique of Olson & Kunasz (1987) for determining the formal solution of Equation (15). According to this technique, the polarized radiation field $\boldsymbol{\mathcal{I}}$ at a given point "O" on a stencil of short-characteristic (MOP, see Figure 1) along a given ray direction and frequency point (say x_m) can be written as

$$\boldsymbol{\mathcal{I}}_{\mathrm{O}}(x_m, \mu) = \boldsymbol{\mathcal{I}}_{\mathrm{M}}(x_m, \mu)e^{-\Delta\tau_{\mathrm{MO}}} + \int_0^{\Delta\tau_{\mathrm{MO}}} \left[\boldsymbol{\mathcal{S}}\left(\tau', x_m\right) + \tilde{\boldsymbol{\mathcal{S}}}\left(\tau', x_m, \mu\right)\right] e^{-\tau'}\,d\tau', \qquad (16)$$

where $\Delta\tau_{\rm MO}$ is the optical distance on the segment MO. As in BH04, along a short-characteristic, we use parabolic and linear interpolation for the source vectors $\boldsymbol{\mathcal{S}}$ and $\tilde{\boldsymbol{\mathcal{S}}}$, respectively. The choice of linear interpolation for $\tilde{\boldsymbol{\mathcal{S}}}$ is made in order to obtain a differencing scheme that is less diffusive in the comoving frame (see BH04 for details). With these choices for interpolation, Equation (16) can be rewritten as

$$\begin{aligned}\boldsymbol{\mathcal{I}}_{\rm O}(x_m,\,\mu) &= e^{-\Delta\tau_{\rm MO}}\boldsymbol{\mathcal{I}}_{\rm M}(x_m,\,\mu)\\ &+ \Psi_{\rm M}\boldsymbol{\mathcal{S}}_{\rm M}(x_m) + \Psi_{\rm O}\boldsymbol{\mathcal{S}}_{\rm O}(x_m) + \Psi_{\rm P}\boldsymbol{\mathcal{S}}_{\rm P}(x_m)\\ &+ \Psi'_{\rm M}\tilde{\boldsymbol{\mathcal{S}}}_{\rm M}(x_m,\,\mu) + \Psi'_{\rm O}\tilde{\boldsymbol{\mathcal{S}}}_{\rm O}(x_m,\,\mu),\end{aligned} \tag{17}$$

where $\Psi_{\rm M}$, $\Psi_{\rm O}$, $\Psi_{\rm P}$ are the parabolic interpolation coefficients and $\Psi'_{\rm M}$, $\Psi'_{\rm O}$ are the linear interpolation coefficients. They depend on $\Delta\tau_{\rm MO}$ and $\Delta\tau_{\rm OP}$, where M and P are the upwind and downwind points, respectively. $\boldsymbol{\mathcal{S}}_{\rm M}$, $\boldsymbol{\mathcal{S}}_{\rm O}$, and $\boldsymbol{\mathcal{S}}_{\rm P}$ are the known (previous iterate) source vectors at points M, O, and P, respectively. The $\tilde{\boldsymbol{\mathcal{S}}}$ contain the effects of the velocity field on the formal solution and are given by

$$\tilde{\boldsymbol{\mathcal{S}}}_{\rm M}(x_m,\,\mu) = -\mu\left(\frac{dV}{d\tau}\right)_{\rm M}\left(\frac{\partial\boldsymbol{\mathcal{I}}}{\partial x}\right)_{{\rm M},x_m}, \tag{18}$$

$$\tilde{\boldsymbol{\mathcal{S}}}_{\rm O}(x_m,\,\mu) = -\mu\left(\frac{dV}{d\tau}\right)_{\rm O}\left(\frac{\partial\boldsymbol{\mathcal{I}}}{\partial x}\right)_{{\rm O},x_m}. \tag{19}$$

As in BH04, we discretize the frequency derivative at any depth point O using a local upwind scheme:

$$\left(\frac{\partial\boldsymbol{\mathcal{I}}}{\partial x}\right)_{{\rm O},x_m} = \frac{\boldsymbol{\mathcal{I}}_{\rm O}(x_m,\,\mu) - \boldsymbol{\mathcal{I}}_{\rm O}(x_{m\mp1},\,\mu)}{x_m - x_{m\mp1}}, \tag{20}$$

where the minus sign applies when $\frac{dV}{d\tau} \geqslant 0$ and the plus sign applies when $\frac{dV}{d\tau} < 0$. If the velocity field is monotonically increasing or decreasing, the problem becomes an initial value problem, that is, we have to specify the initial conditions $\frac{\partial\boldsymbol{\mathcal{I}}}{\partial x}$ at the blue or red frequency edge of the line profile. For example, when $\frac{dV}{d\tau} \geqslant 0$ (i.e., monotonically increasing velocities), the frequency grid runs from $-x_{\rm max}$ to $+x_{\rm max}$ (i.e., $x_{m-1} < x_m < x_{m+1}$). At $x = -x_{\rm max}$ we impose the initial condition, namely, $\frac{\partial\boldsymbol{\mathcal{I}}}{\partial x} = 0$, which is accurate enough if unpolarized continuum radiation ($r \neq 0$) is present in the atmosphere or when thermal emission is imposed as a boundary condition at the lower boundary $\tau = T$ (Schuster problem). Once the intensity at $x = -x_{\rm max}$ is known from Equation (22) below, $\frac{\partial\boldsymbol{\mathcal{I}}}{\partial x}$ at the next frequency point can be evaluated using Equation (20). In other words $\frac{\partial\boldsymbol{\mathcal{I}}}{\partial x}$ is evaluated for each frequency once the intensity $\boldsymbol{\mathcal{I}}$ for the previous frequency point is known. In the case of a monotonically decreasing velocity field the order of the frequency grid should be reversed and the initial condition is imposed at $x = +x_{\rm max}$.

For analytic simplicity, we define

$$\begin{aligned}\delta\boldsymbol{\mathcal{I}}_{\rm O}(x_m,\,\mu) &= \Psi_{\rm M}\boldsymbol{\mathcal{S}}_{\rm M}(x_m) + \Psi_{\rm O}\boldsymbol{\mathcal{S}}_{\rm O}(x_m)\\ &+ \Psi_{\rm P}\boldsymbol{\mathcal{S}}_{\rm P}(x_m).\end{aligned} \tag{21}$$

Substituting Equations (18)–(21) into (17), we obtain the short-characteristic formal solution in a moving atmosphere as

$$\begin{aligned}&\left[1 + \Psi'_{\rm O}\mu\left(\frac{dV}{d\tau}\right)_{\rm O}\frac{1}{(x_m - x_{m\mp1})}\right]\boldsymbol{\mathcal{I}}_{\rm O}(x_m,\,\mu)\\ &= e^{-\Delta\tau_{\rm MO}}\boldsymbol{\mathcal{I}}_{\rm M}(x_m,\,\mu) + \delta\boldsymbol{\mathcal{I}}_{\rm O}(x_m,\,\mu)\\ &\quad + \Psi'_{\rm M}\tilde{\boldsymbol{\mathcal{S}}}_{\rm M}(x_m,\,\mu) + \Psi'_{\rm O}\mu\left(\frac{dV}{d\tau}\right)_{\rm O}\frac{\boldsymbol{\mathcal{I}}_{\rm O}(x_{m\mp1},\,\mu)}{(x_m - x_{m\mp1})}.\end{aligned} \tag{22}$$

Notice the additional terms in the above short-characteristic formal solution due to the comoving frame term. When $\frac{dV}{d\tau} = 0$ (static or constantly moving atmospheres), Equation (22) reduces to the usual short-characteristic formal solution formula of the static case.

3.2.2. Diagonal Approximate Λ-operator

To solve the comoving frame transfer equation using the PALI technique, we need to construct the approximate Λ-operator chosen here to be diagonal. To construct $\boldsymbol{\Lambda}^*_{\rm OO}(x,\,\mu)$ we give a unit pulse at the spatial point "O" and allow the information to propagate along the short-characteristic stencil. Now applying Equation (22), we obtain for the 6×6 diagonal $\boldsymbol{\Lambda}^*$ at $x = \mp x_{\rm max}$

$$\boldsymbol{\Lambda}^*_{\rm OO}(\mp x_{\rm max},\,\mu) = \Psi_{\rm O}\boldsymbol{E} + e^{-\Delta\tau_{\rm MO}}\boldsymbol{\mathcal{I}}_{\rm M}(\mp x_{\rm max},\,\mu)\boldsymbol{E}, \tag{23}$$

and for other frequency points

$$\begin{aligned}&\boldsymbol{\Lambda}^*_{\rm OO}(x_m,\,\mu)\\ &= \left[1 + \Psi'_{\rm O}\mu\left(\frac{dV}{d\tau}\right)_{\rm O}\frac{1}{(x_m - x_{m\mp1})}\right]^{-1}\\ &\quad\times\left[\Psi_{\rm O} + e^{-\Delta\tau_{\rm MO}}\boldsymbol{\mathcal{I}}_{\rm M}(x_m,\,\mu)\right.\\ &\quad - \Psi'_{\rm M}\mu\left(\frac{dV}{d\tau}\right)_{\rm M}\frac{\left[\boldsymbol{\mathcal{I}}_{\rm M}(x_m,\,\mu) - \boldsymbol{\mathcal{I}}_{\rm M}(x_{m\mp1},\,\mu)\right]}{(x_m - x_{m\mp1})}\\ &\quad\left.+ \Psi'_{\rm O}\mu\left(\frac{dV}{d\tau}\right)_{\rm O}\frac{\boldsymbol{\Lambda}^*_{\rm OO}(x_{m\mp1},\,\mu)}{(x_m - x_{m\mp1})}\right]\boldsymbol{E}.\end{aligned} \tag{24}$$

The intensity at the upwind point M (i.e., $\boldsymbol{\mathcal{I}}_{\rm M}$) is non-zero, because the unit pulse perturbation at point O produces a residual intensity at point M due to overshooting caused by the use of the parabolic short-characteristic formula for the stencil behind the current stencil MOP (see Figure 1 of Asensio Ramos & Trujillo Bueno 2006). It can be easily evaluated by applying Equation (22) to the stencil behind the current stencil MOP. The $\boldsymbol{\Lambda}^*_{\rm OO}(x,\,\mu)$ given above self-consistently takes into account the effects of the comoving frame term.

3.3. Convergence Properties of the Co-moving Frame Iterative Methods

We consider isothermal, plane-parallel atmospheres of total optical thickness T with lower boundary condition $I(\tau = T, x, +\mu, \phi) = 1$ and upper boundary condition $I(\tau = 0, x, -\mu, \phi) = 0$. For all the studies presented in this paper the isothermal atmosphere is characterized by the following set of input parameters: $T = 10^5$, $r = 10^{-8}$, $\epsilon = 10^{-4}$, $a = 10^{-3}$, and $B_{\nu_0} = 1$. We neglect the effect of depolarizing elastic collisions. We use a logarithmically spaced τ_I-grid with

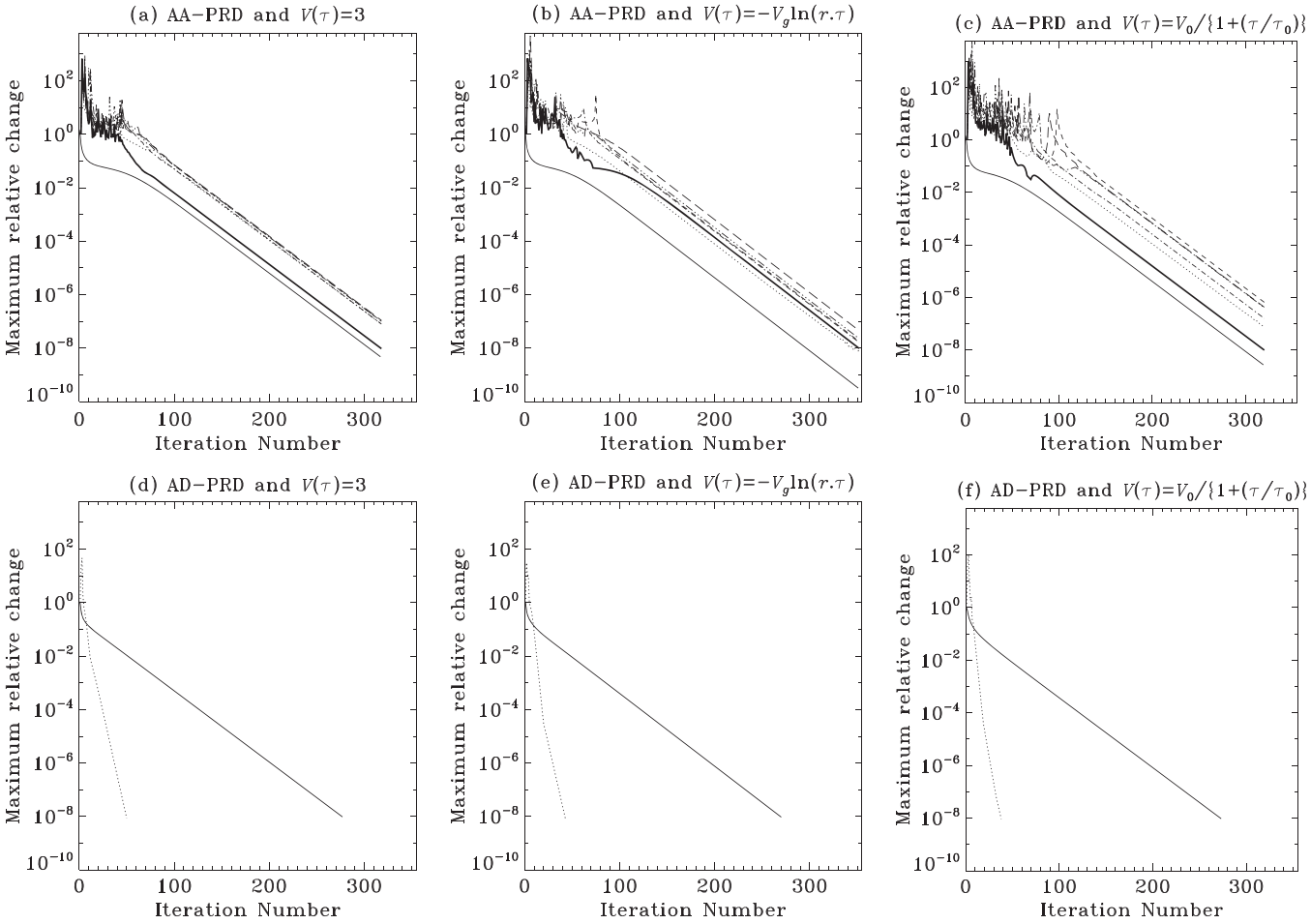

Figure 2. Maximum relative change of comoving frame irreducible source vector components $(c_Q^K)^n$ and of the surface polarization c_p^n as a function of the iteration number. The top row corresponds to the case of angle-averaged PRD (for which a PALI method is used) and the bottom row to the case of angle-dependent PRD (for which SEM is used). The left column corresponds to the case of an atmosphere moving with constant velocity ($V(\tau) = 3$ mean thermal units), the central column to a linear velocity law with $V_g = 0.11$, and the right column to $V(\tau) = V_0/[1 + (\tau/\tau_0)]$, with $V_0 = 3$ and $\tau_0 = 1$. Model parameters are given in Section 3.3. A non-zero magnetic field with parameters $(\Gamma_B, \theta_B, \chi_B) = (1, 30°, 0°)$ is considered. In panels (a)–(c), solid, dotted, dashed, dotted-dashed, dash-triple-dotted, and long-dashed lines correspond to $(c_Q^K)^n$ components and the thick solid line to c_p^n. In panels (d)–(f), the solid line corresponds to $(c_0^0)^n$ and the dotted line to c_p^n.

20 points per decade, with the first depth point at $\tau_{l,1} = 10^{-4}$. For the frequency grid, we use equally spaced points in the line core and logarithmically spaced ones in the wings. Furthermore, the maximum frequency $x_{\max}$ is chosen such that the condition $\varphi(x_{\max})T \ll 1$ is satisfied. We have typically 201 points in the interval $[-x_{\max}, +x_{\max}]$. For the angle grid, we use a seven-point Gauss–Legendre quadrature in the range $[0 < \mu \leqslant 1]$.

The magnetic field strength is parameterized through the Hanle Γ_B parameter, which is defined as $\Gamma_B = g_{J_u}\omega_L/\Gamma_R$, where g_{J_u} denotes the Landé factor of the upper level with total angular momentum quantum number J_u, ω_L is the Larmor frequency, and Γ_R is the radiative width of the upper level. For all the figures presented in this paper we consider a normal Zeeman triplet with $J_u = 1$ and $J_l = 0$. The field inclination and azimuth with respect to the atmospheric normal are denoted by θ_B and χ_B, respectively.

To study the convergence properties of the comoving frame method, we plot in Figure 2 the maximum relative change of the irreducible source vector components $(c_Q^K)^n$ and of the surface polarization c_p^n as a function of the iteration number. We use the same definition of $(c_Q^K)^n$ and c_p^n as given for example in Equations (38)–(40) of Sampoorna et al. (2011). For the PALI method the iterations are stopped when $\max\left[(c_0^0)^n, c_p^n\right] < 10^{-8}$. For the SEM, two iteration tests are performed: the first one on $(c_0^0)^n$ when calculating the component $\tilde{I}_0^{(0)0}$ using an ALI method, and the second one on c_p^n when calculating the polarized components (see Nagendra & Sampoorna 2011; Sampoorna et al. 2011, for more details). In this case the iterations are stopped when $(c_0^0)^n$ and c_p^n become smaller than 10^{-8}.

For both the PALI and SEM, the convergence behavior of a constantly moving atmosphere is identical to that of the static atmosphere, because in this case the velocity gradient is zero and the comoving frame transfer equation has the same form as that for the static case. In the case of the PALI method, the convergence rate of the $(c_Q^2)^n$ components is somewhat reduced when velocity gradients are present in the medium (see panels (b) and (c)). Further, several sharp peaks persist as far as 100 iterations. This can be attributed to the effect of the comoving frame term in Equation (10). For the SEM, the convergence behavior seems to be somewhat less sensitive to the choice of velocity law. Finally we remark that for practical applications it is safe to stop the iterations when the maximum relative change is less than 10^{-4} (which is also evident from Figure 2).

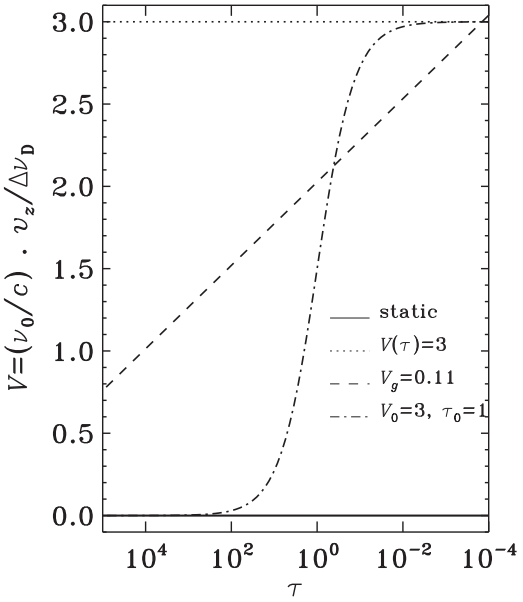

Figure 3. Non-dimensional velocity field $V(\tau)$ as a function of τ. The solid line corresponds to the static case, the dotted line to $V(\tau) = 3$ mean thermal units, the dashed line to a linear velocity law with $V_g = 0.11$, and the dotted-dashed line to $V(\tau) = V_0/[1 + (\tau/\tau_0)]$, with $V_0 = 3$ and $\tau_0 = 1$.

4. NUMERICAL RESULTS

Here we present the emergent Stokes profiles computed for different empirical velocity laws (see Section 4.1). We consider both the non-magnetic (see Section 4.2) and magnetic cases (see Section 4.3). We compare the profiles computed with CRD, angle-averaged PRD, and the angle-dependent PRD. The static case solution is always shown as a solid line for reference and comparison.

4.1. Empirical Velocity Laws

The non-dimensional velocity V is specified on the line optical depth grid τ_l. For brevity of notation, hereafter we refer to τ_l as τ itself. For our studies, we consider moving atmospheres with three types of empirical velocity laws. The first one is an isothermal atmosphere moving with constant velocity toward the observer (i.e., $V(\tau) =$ constant). The second one is an atmosphere having a velocity law given by

$$V(\tau) = -V_g \ln(r\tau), \tag{25}$$

where V_g represents the constant velocity gradient. A positive velocity gradient is assumed for all the studies, so that the atmosphere is again moving toward the observer, but different layers are moving with different vertical velocities. For an exponentially stratified atmosphere, the velocity law given by Equation (25) corresponds to a linear variation of velocity with height. Therefore we refer to this velocity law as the linear velocity law. The third one is an atmosphere with a velocity law given by (see Mihalas 1978)

$$V(\tau) = V_0/\big[1 + (\tau/\tau_0)\big], \tag{26}$$

with V_0 being the limiting value of velocity at small optical depths (i.e., $V_0 = V(\tau \to 0)$), and τ_0 gives the location in optical depth of the region of largest velocity gradient. Again $V(\tau)$ is taken to be positive outward through the atmosphere. The nature of these three vertical velocity fields as a function of optical depth τ is shown in Figure 3.

4.2. Scattering Polarization Profiles: the Non-magnetic Case

Here we present the emergent Stokes profiles formed in an isothermal atmosphere in the absence of magnetic fields and with different velocity laws discussed in Section 4.1. Figures 4 and 5 show the emergent (I, Q/I) profiles for limb distances $\mu = 0.13$ and $\mu = 0.7$, respectively. The solutions computed with CRD, angle-averaged PRD, and angle-dependent PRD are shown in panels (a)–(c), respectively. A strong absorption line with broad damping wings is seen in the CRD intensity profile. In addition, the PRD I profiles exhibit a self-reversed absorption line with even broader damping wings.

The velocity fields have two main effects on polarized line formation. The first is the Doppler shift, which manifests itself in the formal solution. The second is the so-called radiation trapping or escape, which arises due to the change of the scattering integral and thereby the source vector. This leads to the so-called Doppler brightening or dimming effect. The effect of the Doppler shift can be clearly seen in the (I, Q/I) profiles, which are shifted toward the blue. This shift is larger for a nearly vertical ray ($\mu = 0.7$) than for a horizontal ray ($\mu = 0.13$). This is expected as the Doppler shift is given by $x - \mu V$. A constantly moving atmosphere only produces a Doppler shift, while an atmosphere with velocity gradient not only produces a Doppler shift of the profiles but also enhances the linear polarization compared to the static and constantly moving atmospheres. As explained in detail in Carlin et al. (2012) the enhancement in Q/I arises due to an enhancement in anisotropy that is caused by the Doppler brightening effect. This enhancement in Q/I is seen for both the vertical and horizontal rays, unlike the Doppler shift which is predominant mainly for a vertical ray in a plane-parallel atmosphere with vertical velocity fields. Furthermore, the enhancement in Q/I is progressively larger for angle-averaged and angle-dependent PRD compared to the CRD case.

To further clarify the Doppler brightening or dimming effect, in Figure 6 we show a plot of mean intensity ($\bar{J}^0_0$) and the radiation anisotropy (defined as $\bar{J}^2_0/\bar{J}^0_0$) as a function of line optical depth τ_l (denoted by τ for brevity of notation) for $\mu = 0.13$. The components of the mean intensity vector $\bar{J}^K_Q$ are given by the right-hand side of Equation (7) without the contribution from the thermal term. In the case of CRD $\bar{J}^K_Q$ depends only on τ for both the static and moving atmospheres. On the other hand, for the case of angle-averaged PRD, $\bar{J}^K_Q$ depends on τ and x for a static atmosphere, and on τ, x, and μ for a moving atmosphere. In the non-magnetic case $\bar{J}^0_0$ and $\bar{J}^2_0$ are the only non-zero components of the mean intensity vector. Figure 6(a) shows $\bar{J}^0_0$ and $\bar{J}^2_0/\bar{J}^0_0$ for CRD (gray lines) and for angle-averaged PRD at $x = 0$ (black lines). Clearly the mean intensity vectors for CRD and angle-averaged PRD nearly coincide at $x = 0$.

The mean intensity and radiation anisotropy coincide for static and constantly moving atmosphere (see solid and dotted lines in Figure 6(a)). For velocity laws with non-zero velocity gradient $\bar{J}^0_0$ and $\bar{J}^2_0/\bar{J}^0_0$ in the surface layers are higher than in the corresponding static case. This is the effect of Doppler brightening. It occurs because the atoms in the higher layers that are moving with larger velocity intercept more effectively the radiation from the blue wing photons emerging from the deeper layers. Since the wings of an absorption line have a

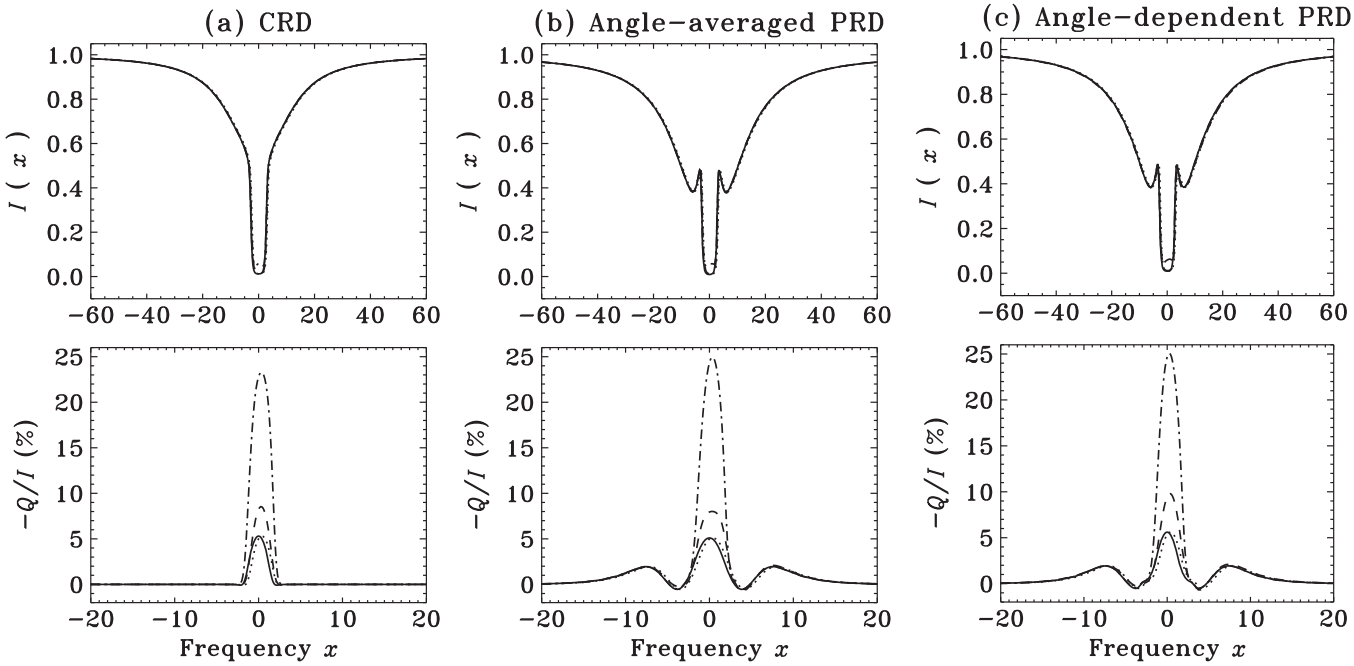

Figure 4. Emergent intensity I and linear polarization Q/I profiles at $\mu = 0.13$ for an absorption line formed in an isothermal atmosphere with the following model parameters: $T = 10^5$, $\epsilon = 10^{-4}$, $a = 10^{-3}$, $r = 10^{-8}$, $B_{\nu_0} = 1$. Panels (a)–(c), respectively, show the solutions computed with CRD, angle-averaged PRD, and angle-dependent PRD. Different line types are computed with the corresponding velocity laws shown in Figure 3.

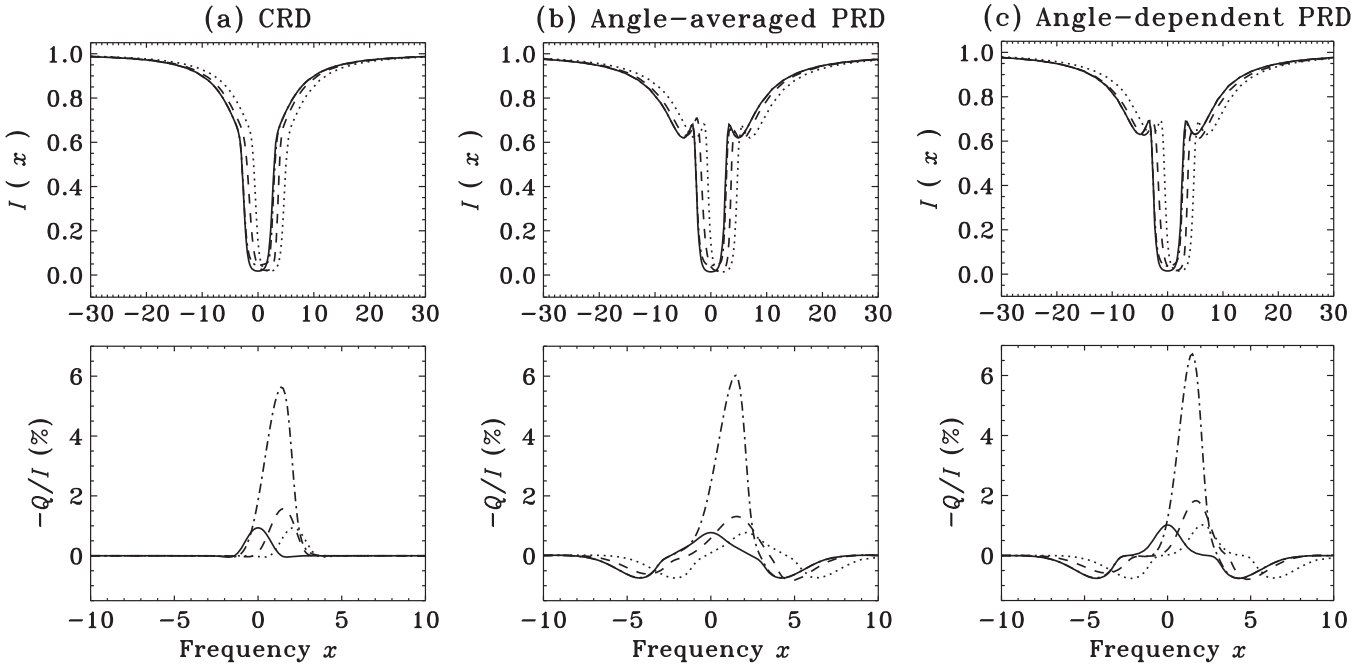

Figure 5. Same as Figure 4 but for a nearly vertical ray with $\mu = 0.7$.

greater intensity than the core, this leads to larger values of $\bar{J}^0_0$ in the higher layers than in the static case. Also, because the projected velocity (μV) is larger for the vertical rays than the horizontal rays, Doppler brightening is predominant for vertical rays. This introduces an additional limb-darkening and thereby an increase in anisotropy ($\bar{J}^2_0/\bar{J}^0_0$).

The above discussion is valid for the case of CRD and angle-averaged PRD at $x = 0$. This is because at $x = 0$ the angle-averaged type II redistribution function can be approximated by the CRD function. This is no longer the case for line wing frequencies. It is well known that the angle-averaged type II redistribution function $R_{\rm II}(x, x')$ for the static case has coherent peaks at $x \approx x'$. In the case of moving atmospheres $R_{\rm II}(x - \mu V, x' - \mu' V)$ has peaks at $(x - \mu V) \approx (x' - \mu' V)$, thereby coupling the incoming and outgoing rays not only in frequency but also in direction due to the velocity field. Thus the mean intensity vector $\bar{J}^K_0$ would show a complicated behavior in the line wings. For $x = +3.75$ (see black lines in Figure 6(b)) $\bar{J}^0_0$ for all the three types of velocity laws nearly coincide with the static case, while we see a Doppler dimming

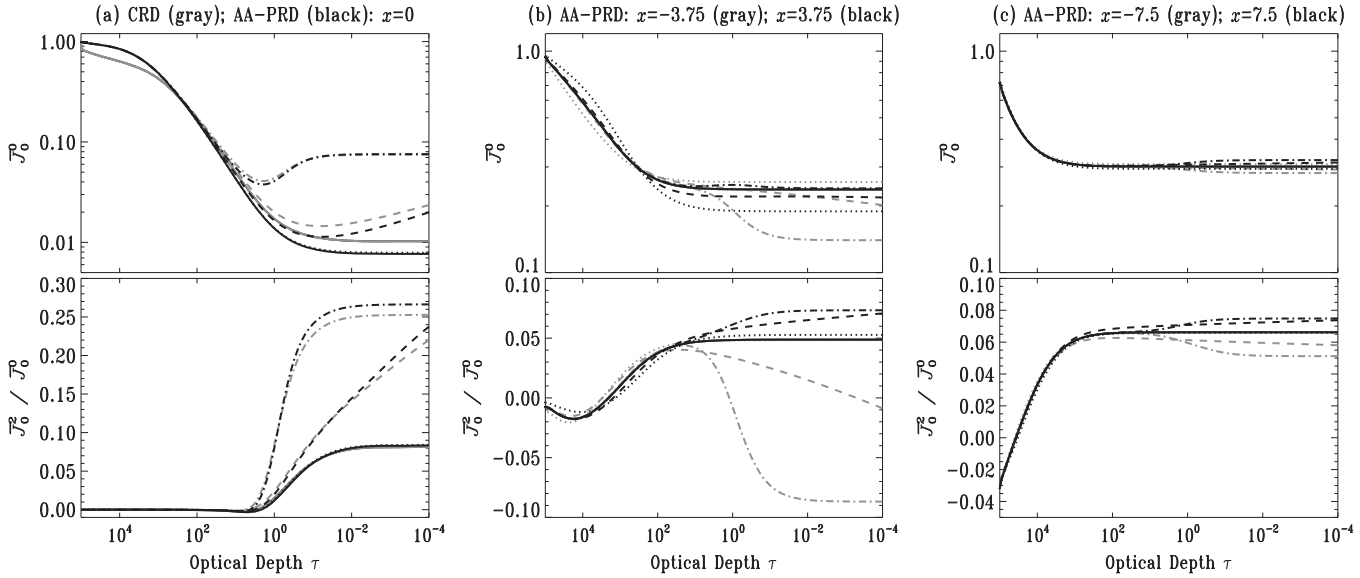

Figure 6. Mean intensity $\bar{J}^0_0$ and the radiation anisotropy ($\bar{J}^2_0/\bar{J}^0_0$) at $\mu = 0.13$. The model parameters are the same as those used in Figure 4. The mean intensity vectors for the case of CRD (gray lines) and angle-averaged PRD (black lines) at $x = 0$ are shown in panel (a). Panels (b) and (c), respectively, show the mean intensity vector for angle-averaged PRD at $|x| = 3.75$ (corresponding to the core minimum) and $|x| = 7.5$ (corresponding to the PRD wing peak). In these panels the gray lines correspond to $-x$ and black lines to $+x$. Different line types are computed with the corresponding velocity laws shown in Figure 3.

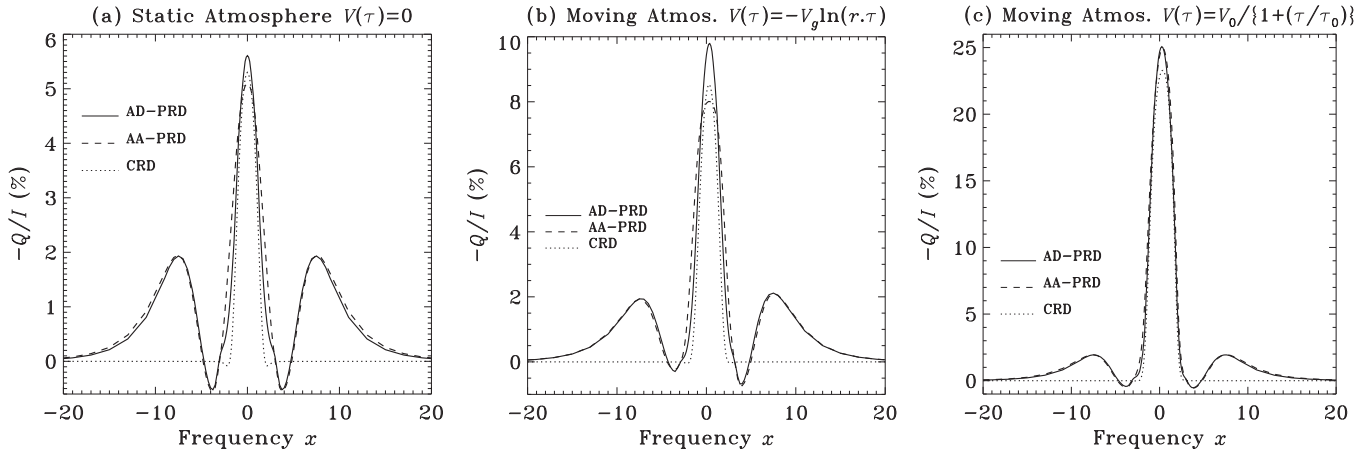

Figure 7. Comparison of emergent Q/I profiles at $\mu = 0.13$, computed with angle-dependent PRD (AD-PRD), angle-averaged PRD (AA-PRD), and CRD. Panels (a)–(c) correspond respectively to a static atmosphere, and moving atmospheres with the velocity laws given by Equations (25) and (26). The other model parameters are the same as in Figure 4.

effect for $x = -3.75$, especially for the velocity law given by Equation (26) (see gray dotted-dashed line in Figure 6(b)). The anisotropy increases in higher layers for $x = +3.75$, while it decreases for $x = -3.75$ compared to the static case. We remark that $x = \pm 3.75$ correspond to minima between the core peak and PRD wing peaks (hereafter core minima) in the Q/I profile (see Figure 4(b)). This difference in anisotropy between the blue and red core minima is reflected clearly in the Q/I profile for the case of a linear velocity law (see Figure 7(b)). In the case of a velocity law given by Equation (26) also, there exists very slight asymmetry in the blue and red core minima of the Q/I profile, although it is not clearly visible in the scale adopted (see Figure 7(c)).

For $x = |7.5|$, which corresponds to a wing PRD peak in the Q/I profile (see Figure 4(b)), $\bar{J}^0_0$ for all the cases nearly coincide, while anisotropy shows a slight enhancement in higher layers for $x = +7.5$ and a slight decrease again in higher layers for $x = -7.5$ compared to the static case. This slight difference in anisotropy between the blue and red wing PRD peaks would lead to a slight asymmetry in the Q/I PRD wing peak, although it is too small to be seen graphically.

From Figure 3, we see that in the case of a velocity law given by Equation (26), deeper layers are nearly static and layers in the optical depth range $10^2 > \tau \geq 10^{-4}$ are moving progressively with increasing velocity toward the observer, until the limiting value of V_0 is reached. Thus the effect of the velocity law given by Equation (26) is mainly seen in the line core, which is formed in higher layers. The effects of linear velocity law on the Q/I profile can be seen more clearly by comparing solid lines in Figures 7(a) and (c) for $\mu = 0.13$ and Figures 8(a) and (c) for $\mu = 0.7$. Clearly, the core minima on the blue and red sides have become asymmetric. As for the PRD wing peaks, there is a very slight asymmetry between the blue and red wing peaks, although not graphically discernable. This asymmetry is caused by the asymmetry in the line opacities between the blue and red wings of the line profile due to the

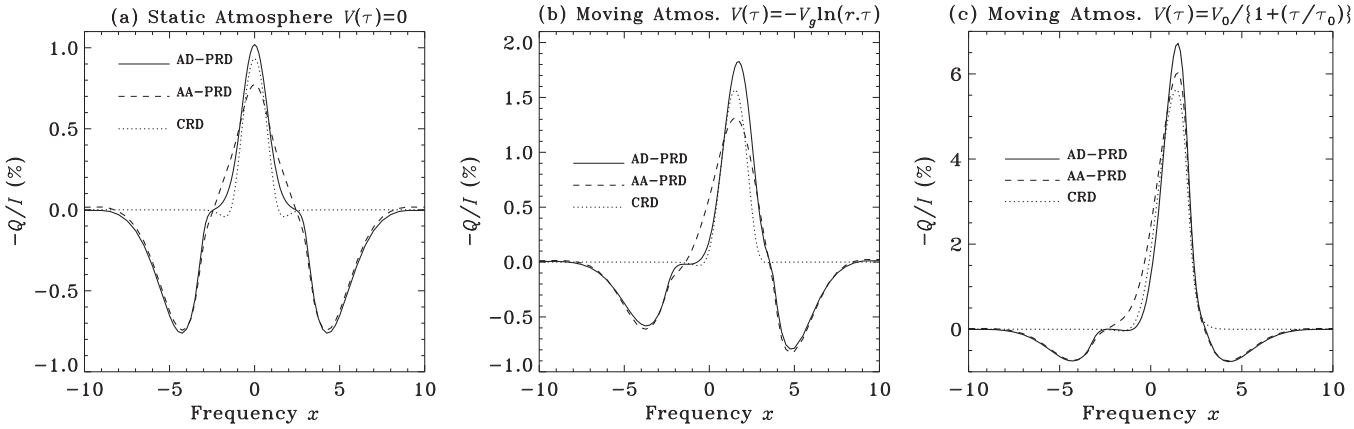

Figure 8. Same as Figure 7 but for $\mu = 0.7$.

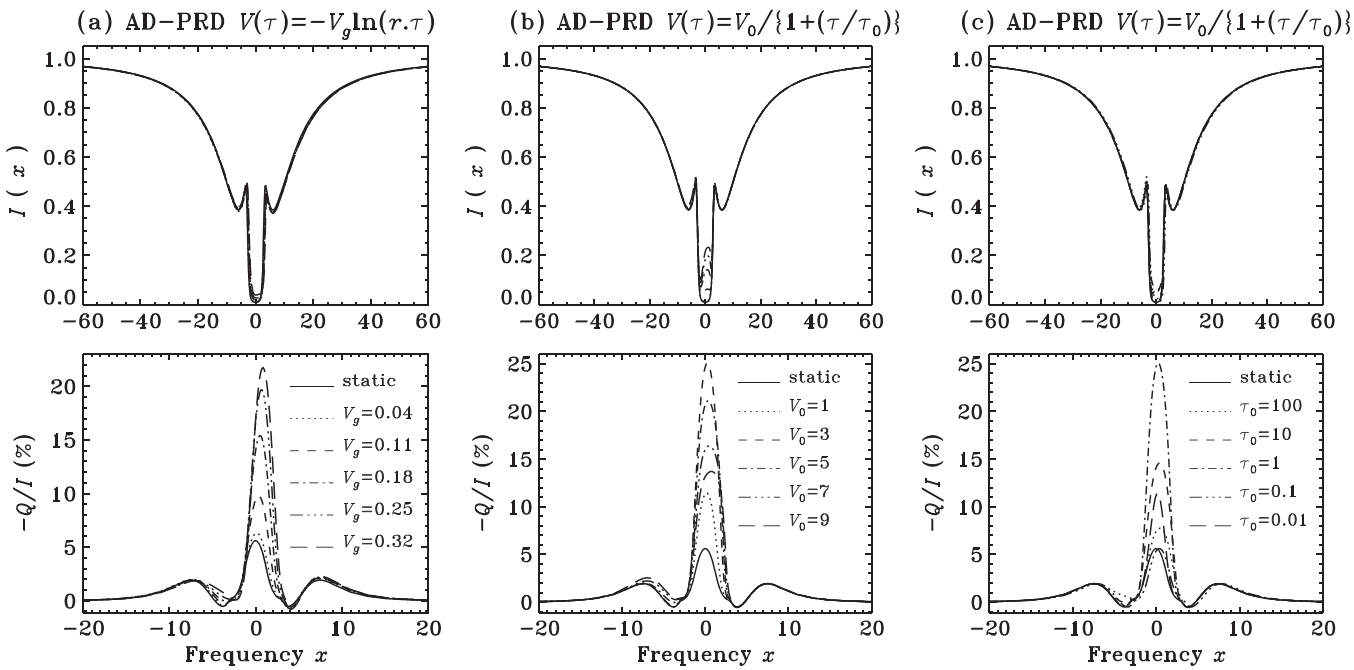

Figure 9. I and Q/I profiles at $\mu = 0.13$ emerging from a moving atmosphere with linear velocity law (panel (a)) and with a velocity law given by Equation (26) (panels (b) and (c)). Angle-dependent PRD is used. In panel (b) $\tau_0 = 1$, while in panel (c) $V_0 = 3$. Other model parameters are the same as in Figure 4.

Doppler shift. Clearly, the photons in the blue wing are more efficiently trapped than those in the red wing, because of the larger opacity in the blue wing (we have given a blueshift to the medium). This leads to larger anisotropy in the blue wings than the red (see Figures 6(b) and (c)). It is interesting to note that the observed Q/I profiles of the Ca I 4227 Å line exhibit such asymmetries in the PRD wing peaks and the core minima (see, e.g., Gandorfer 2002). Although the asymmetric PRD wing peaks could be accounted for in the theoretical model profiles through the use of blend line opacity and elastic collisions, the asymmetry in the core minima has not been accounted for (see, e.g., Anusha et al. 2010; Supriya et al. 2014).

Figures 7 and 8 show a comparison between the emergent Q/I profiles computed with angle-dependent PRD (solid lines), angle-averaged PRD (dashed lines), and CRD (dotted lines) for $\mu = 0.13$ and $\mu = 0.7$, respectively. The typical differences between the CRD and PRD intensity profiles are clearly seen in the top panels of Figures 4 and 5. Therefore in Figures 7 and 8 we present only the Q/I profiles. In general the Q/I profiles computed with CRD are confined to the line core and are slightly narrower than those computed with angle-averaged and angle-dependent PRD. However, in the case of a moving atmosphere with velocity law given by Equation (26), Q/I profiles computed with different redistribution mechanisms nearly coincide in the line core. The differences between Q/I profiles computed with angle-averaged and angle-dependent PRD are of similar nature for both a static atmosphere and the moving atmospheres. For a horizontal ray the differences are negligible, while for a vertical ray some differences in the line core region are seen. Thus, for optically thick lines, the angle-averaged PRD can be safely used for the computation of Q/I profiles, irrespective of whether the atmosphere is moving or static.

Figures 9 and 10 show the Stokes profiles emerging from a moving atmosphere with velocity laws given by Equations (25) and (26) again for $\mu = 0.13$ and $\mu = 0.7$, respectively. Angle-dependent PRD is used in the computations. Panels (a) show the effect of varying the velocity gradient V_g, panels (b)

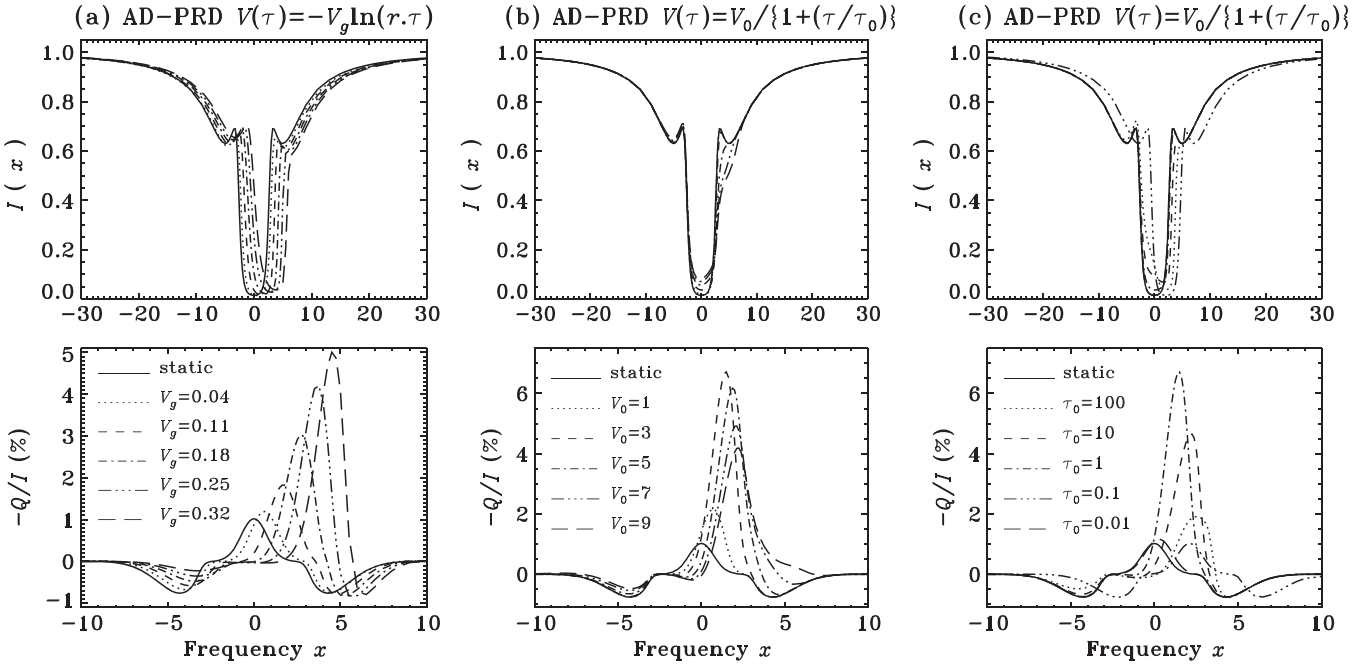

Figure 10. Same as Figure 9 but for $\mu = 0.7$.

that of V_0, and panels (c) that of τ_0. For the case of the linear velocity law, the different values of V_g are chosen such that the velocity at the surface is nearly the same as V_0 used for panel (b). To give the reader an idea of the actual value of macroscopic velocity v_z in physical units, we convert the non-dimensional velocity V to v_z by taking the example of the Ca I 4227 Å line formed in an atmosphere of temperature 6000 K. The non-dimensional velocity V is given by $V = v_z/\sqrt{v_{\rm th}^2 + v_{\rm turb}^2}$ where $v_{\rm th}$ is the mean thermal velocity and $v_{\rm turb}$ is the microturbulent velocity. At 6000 K, $v_{\rm th}$ for Ca I atoms is 1.58 km s^{-1}. Assuming a $v_{\rm turb}$ of 2 km s^{-1}, the actual macroscopic velocities corresponding to $V_0 = [1, 3, 5, 7, 9]$ are $v_z = [2.54, 7.64, 12.73, 17.83, 22.92]$ km s^{-1}, respectively. Velocities of this magnitude are quite common in stellar atmospheres.

For the intensity profiles, larger effects are seen for a vertical ray than for a horizontal ray irrespective of the velocity law used. We now discuss the Q/I profiles computed with the linear velocity law (see Figures 9(a) and 10(a)). For Q/I profiles at $\mu = 0.13$, the asymmetry in the blue and red core minima increases with increasing $V_{\rm g}$, while the asymmetry in the PRD wing peaks starts to show up marginally. Further, the magnitude of the line center peak in Q/I increases with increasing $V_{\rm g}$. In the case of the Q/I profile at $\mu = 0.7$, the PRD wing peaks are highly suppressed (due to the center-to-limb behavior of the scattering polarization profiles), and thereby the core minimum appears as a negative peak (see Figure 10(a)). As the velocity gradient ($V_{\rm g}$) increases, the asymmetry in the blue and red core minima peak increases considerably. Also the Q/I profiles are progressively Doppler-shifted with increasing line center amplitudes.

For the velocity law given by Equation (26), the effect of varying V_0 and τ_0 is mainly seen in the line core of (I, Q/I) profiles for a horizontal ray (see Figures 9(b) and (c)), while it is also seen predominantly in the blue wing region for a vertical ray (see Figures 10(b) and (c)) due to the Doppler shifts. Q/I initially increases with increasing V_0, reaches a maximum for $V_0 = 3$, and then decreases with further increase in V_0. This behavior is similar to that discussed in Carlin et al. (2012), who show that the decrease in Q/I for $V_0 > 3$ is due to the increased negative contribution from the horizontal rays to the anisotropy. The dependence of Q/I profiles on τ_0 is somewhat similar to that on V_0, that is, Q/I initially increases as τ_0 decreases, reaches a maximum for $\tau_0 = 1$, and then decreases with further decrease in τ_0 (see Figures 9(c) and 10(c)).

Velocity fields are quite common in stellar atmospheres. Therefore it is essential to take them into account in the computation of linear polarization profiles formed in the absence of magnetic fields. This is because they serve as a reference when determining the combined effects of velocity and magnetic fields in Hanle diagnostics.

4.3. Scattering Polarization Profiles: the Case of the Hanle Effect

Here we present studies similar to those presented in Section 4.2 but for the presence of a weak magnetic field. Figures 11–16 show the magnetic analogue of Figures 4, 5, 7–10. For these figures the magnetic field parameters are chosen to be $\Gamma_B = 1$, $\theta_B = 30°$, and $\chi_B = 0°$.

The Stokes intensity I profiles are marginally affected by a weak field, and hence they are not shown here. We now compare the non-magnetic Q/I profiles shown in Figures 4 and 5 with the corresponding magnetic Q/I profiles shown in Figures 11 and 12. The shapes of the Q/I profiles for both magnetic and non-magnetic cases are nearly the same, except for a Hanle depolarization in the line core which is larger in a moving atmosphere than in a static atmosphere (see also Figure 17). In the case of a velocity law given by Equation (26) and angle-dependent PRD, we notice the appearance of an additional peak in the red wing region of the core minima for both horizontal and vertical rays (see dotted-dashed lines in Figures 11(c) and 12(c); also compare solid lines in Figures 7(c) and 13(c) and those in Figures 8(c) and 14(c)). In the case of a linear velocity law and angle-dependent PRD,

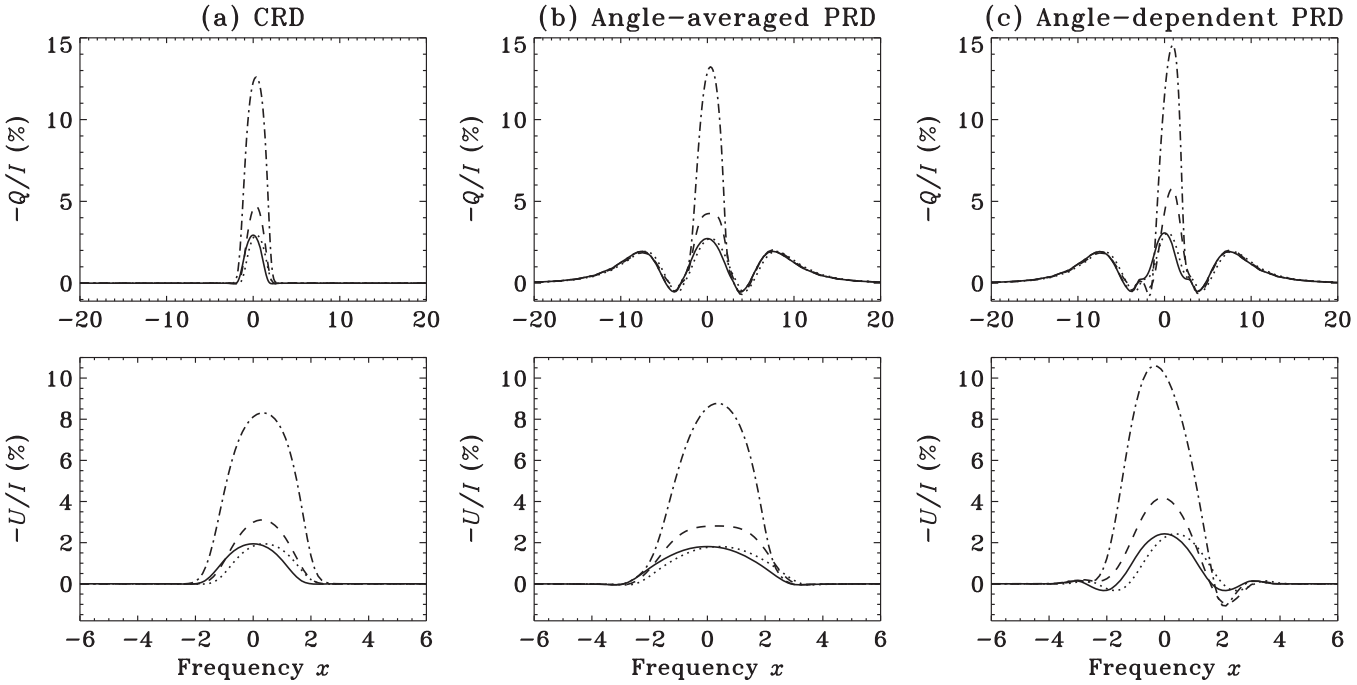

Figure 11. Emergent Q/I and U/I profiles at $\mu = 0.13$ computed in the presence of a weak magnetic field parameterized as (Γ_B, θ_B, χ_B) = (1, 30°, 0°). Other model parameters and the line types are the same as in Figure 4.

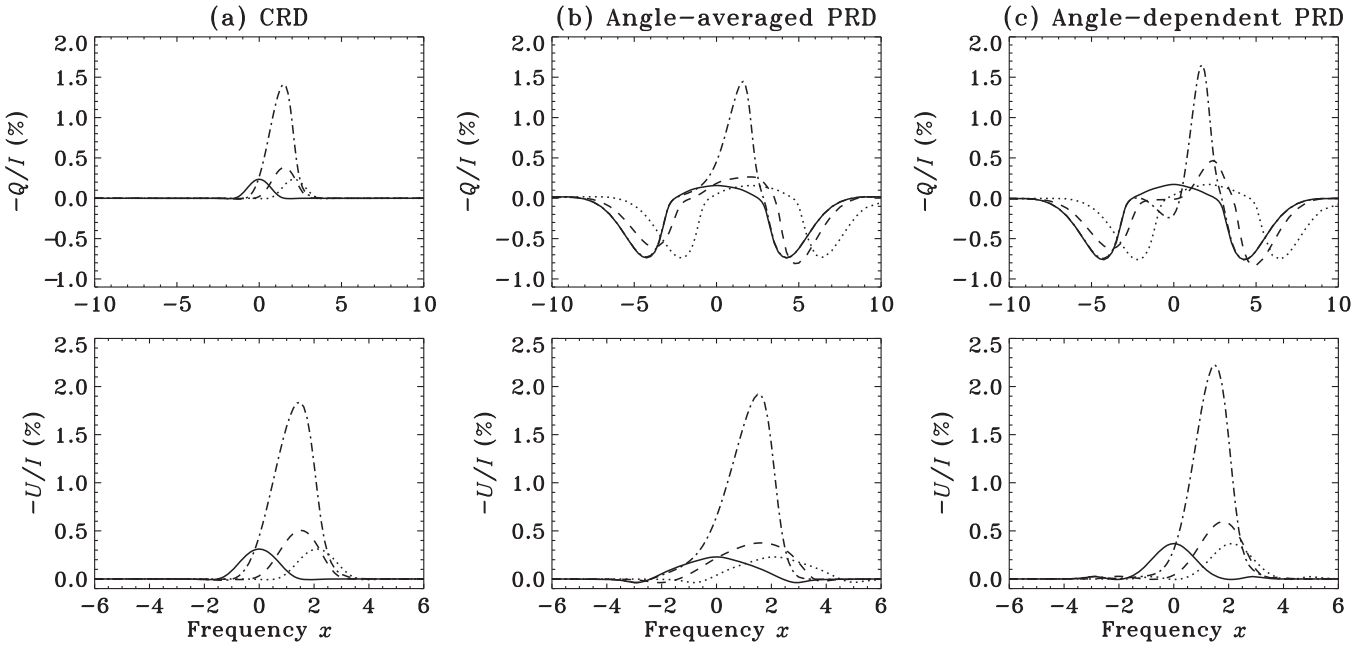

Figure 12. Same as Figure 11 but for $\mu = 0.7$.

we notice also this additional small peak but only for the horizontal ray (see dashed line in Figure 11(c) and solid line in Figure 13(b)). The Stokes U/I profiles are generated due to Hanle rotation. Like the Q/I profiles they are very sensitive to the vertical velocity gradients, that is, they are larger in magnitude than in the static case, asymmetric about the line center, and also exhibit a Doppler shift, particularly visible for the vertical ray (see Figures 11 and 12).

From Figures 13 and 14, we see that the comparison between the Q/I profiles computed with CRD, angle-averaged, and angle-dependent PRD are similar to those observed for the non-magnetic case. Unlike the Q/I profiles, the U/I profiles are quite sensitive to the choice of the frequency redistribution mechanism, because they are generated from breaking of the azimuthal symmetry. Clearly, the angle-dependent PRD effects are more important for the U/I profiles not only in the static case but also when vertical velocity gradients are present in the atmosphere.

Comparing Figures 15 and 16 with the corresponding Figures 9 and 10 for the non-magnetic case, we see that the dependence of both the Q/I and U/I profiles on the vertical velocity gradient in the case of a linear velocity law and on V_0

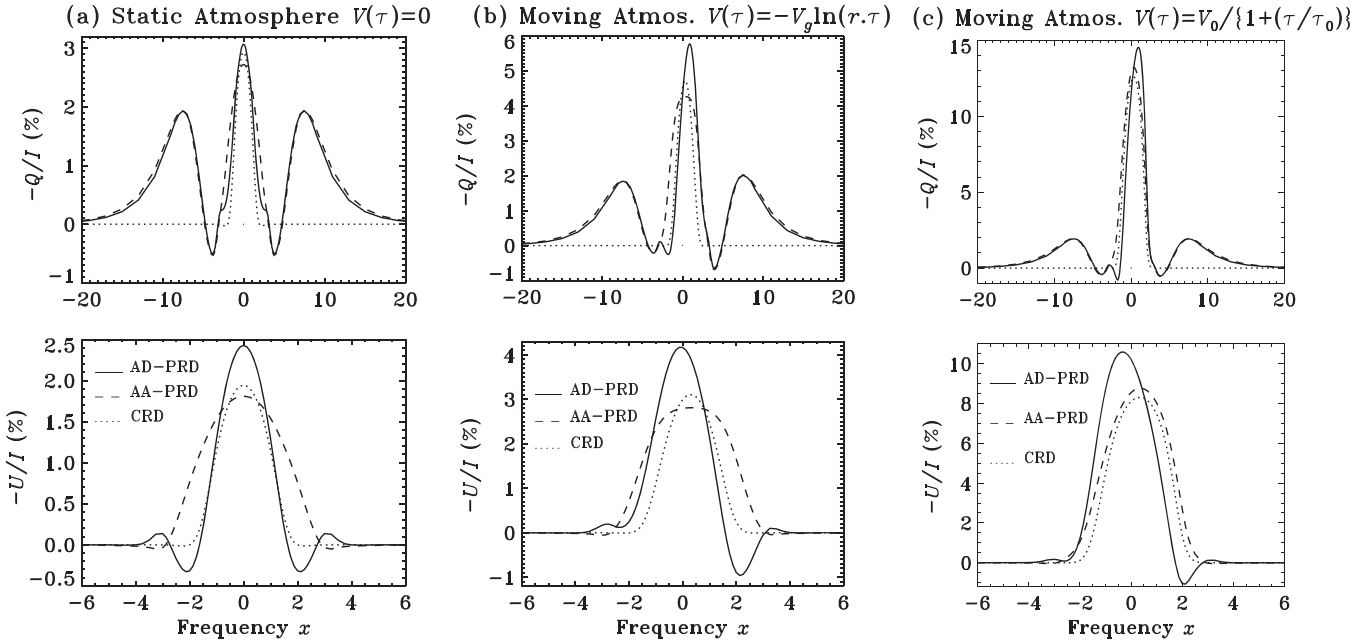

Figure 13. Comparison of emergent Q/I and U/I profiles at $\mu = 0.13$, computed with angle-dependent PRD (AD-PRD), angle-averaged PRD (AA-PRD), and CRD. Panels (a)–(c) correspond, respectively, to a static atmosphere, and moving atmospheres with the velocity laws given by Equations (25) and (26). The other model parameters are the same as in Figure 11.

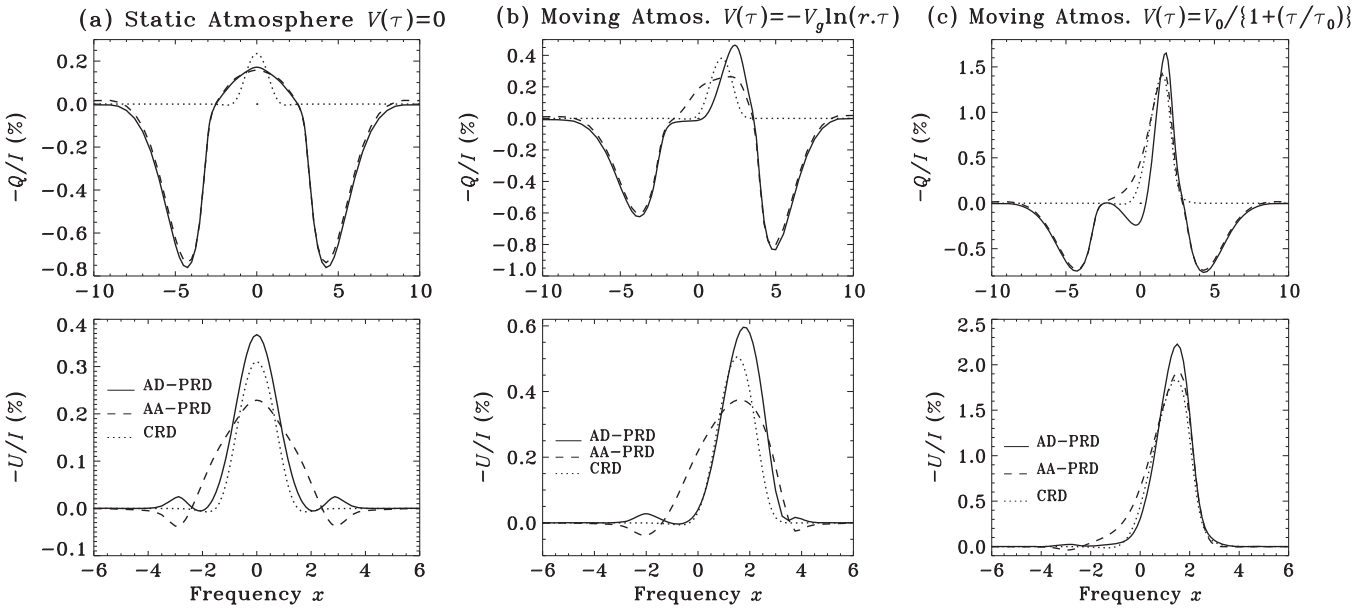

Figure 14. Same as Figure 13 but for $\mu = 0.7$.

and τ_0 in the case of a velocity law given by Equation (26) is similar to those exhibited by the corresponding non-magnetic Q/I profiles. We remark that, even in the moving atmosphere, the Hanle effect continues to operate in the line core. However, due to Doppler shift of the profiles, Hanle depolarization is seen in the Doppler-shifted line core (for example, compare Q/I panels in Figures 10 and 16), and the entire U/I profiles shift toward the blue (see example U/I panels in Figure 16(a)).

To demonstrate the importance of velocity fields in Hanle diagnostics, in Figure 17 we show a comparison of Stokes profiles computed with and without magnetic field for a nearly vertical ray. For this purpose it is sufficient to consider the angle-averaged PRD matrix. Irrespective of whether the atmosphere is moving or static, the Hanle effect vanishes for a vertical magnetic field ($\theta_B = 0$). As a result the solid and dotted lines in Figure 17 are indistinguishable. Comparing the line core peak amplitudes of Q/I profiles for magnetic and non-magnetic cases (compare for example solid and dashed lines in Figure 17), we see that the amount of Hanle depolarization is larger for a moving atmosphere than for the static case. Further, as already noted above, the magnitudes of the U/I profiles are larger for a moving atmosphere than their static counterparts. Clearly, if one tries to infer the magnetic field from these Q/I and U/I profiles (say, dashed lines in Figures 17(b) and (c)) while neglecting the velocity field effects then one would either (a) mis-diagnose the magnetic field if the profiles are

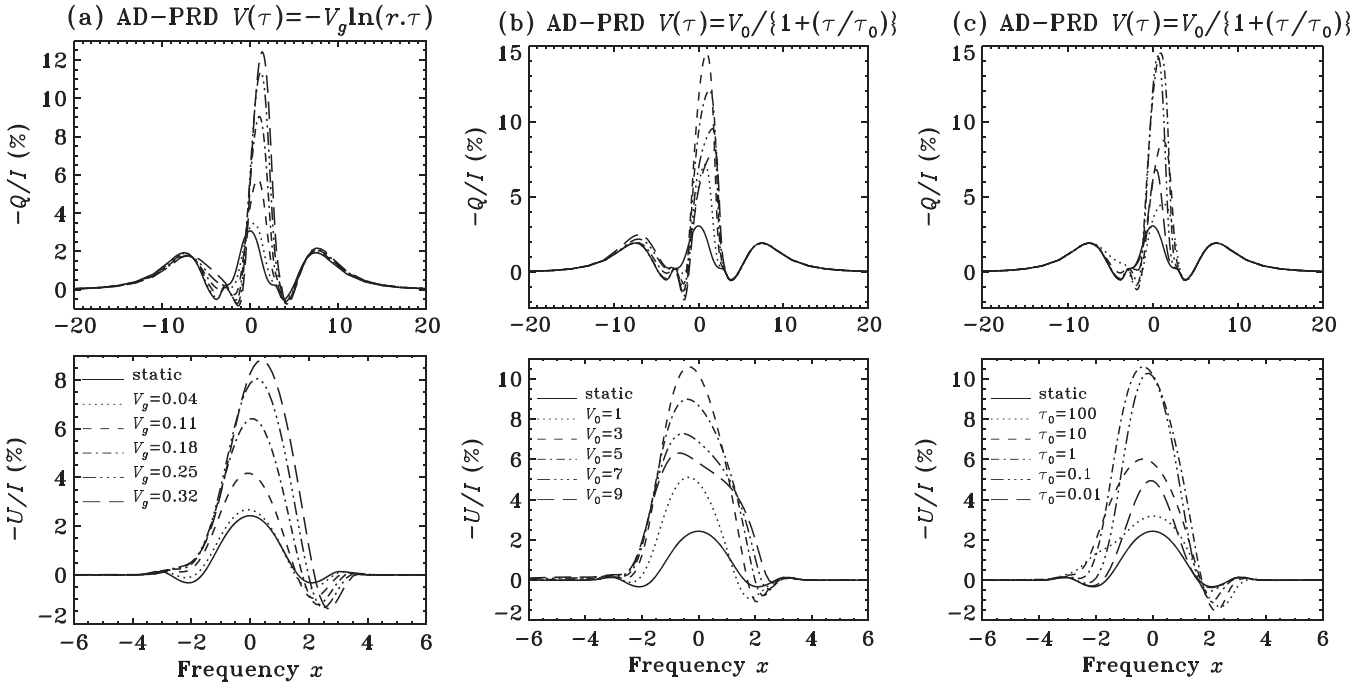

Figure 15. Q/I and U/I profiles at $\mu = 0.13$ emerging from a moving atmosphere with a linear velocity law (panel (a)) and with a velocity law given by Equation (26) (panels (b) and (c)). Angle-dependent PRD is used. Other model parameters are the same as in Figure 9 except for the presence of a weak magnetic field.

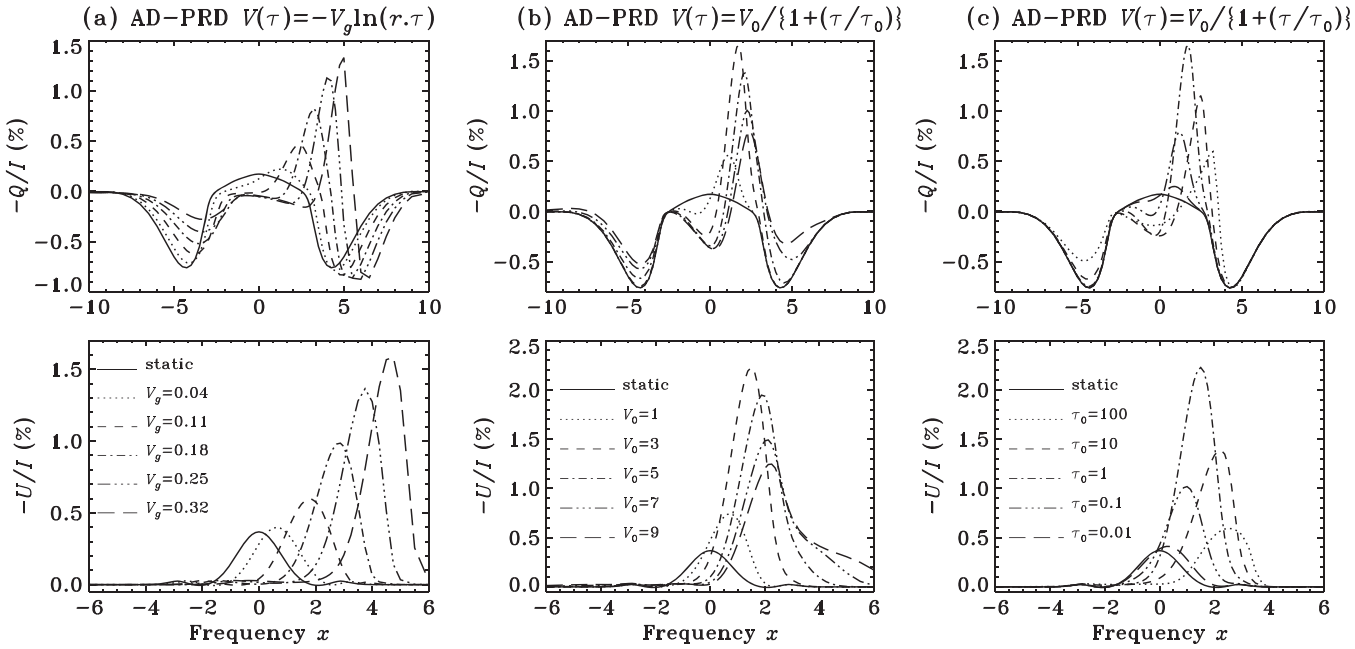

Figure 16. Same as Figure 15 but for $\mu = 0.7$.

reproduced fully or (b) infer the need for multi-dimensional effects if the profiles are not reproduced in full detail. Thus care should be taken when interpreting the observations from a region on the Sun where both the magnetic and velocity fields operate together (say in a solar prominence).

5. CONCLUSIONS

For a correct interpretation of the linear polarization profiles emerging from solar or stellar atmospheres, it is essential to take into account the dynamical state of the atmosphere, apart from accounting for scattering physics (such as PRD, quantum interference, etc.) and magnetic fields. In this paper we have presented comoving frame methods to solve the polarized line transfer equation in the presence of velocity and magnetic fields. We consider planar isothermal atmospheres with vertical velocity fields, and with CRD, angle-averaged, and angle-dependent PRD as the frequency redistribution mechanisms for scattering on a two-level atom with unpolarized ground level. We have shown that the comoving frame methods are far superior when compared to the observer's frame method in terms of both computational speed and memory requirements.

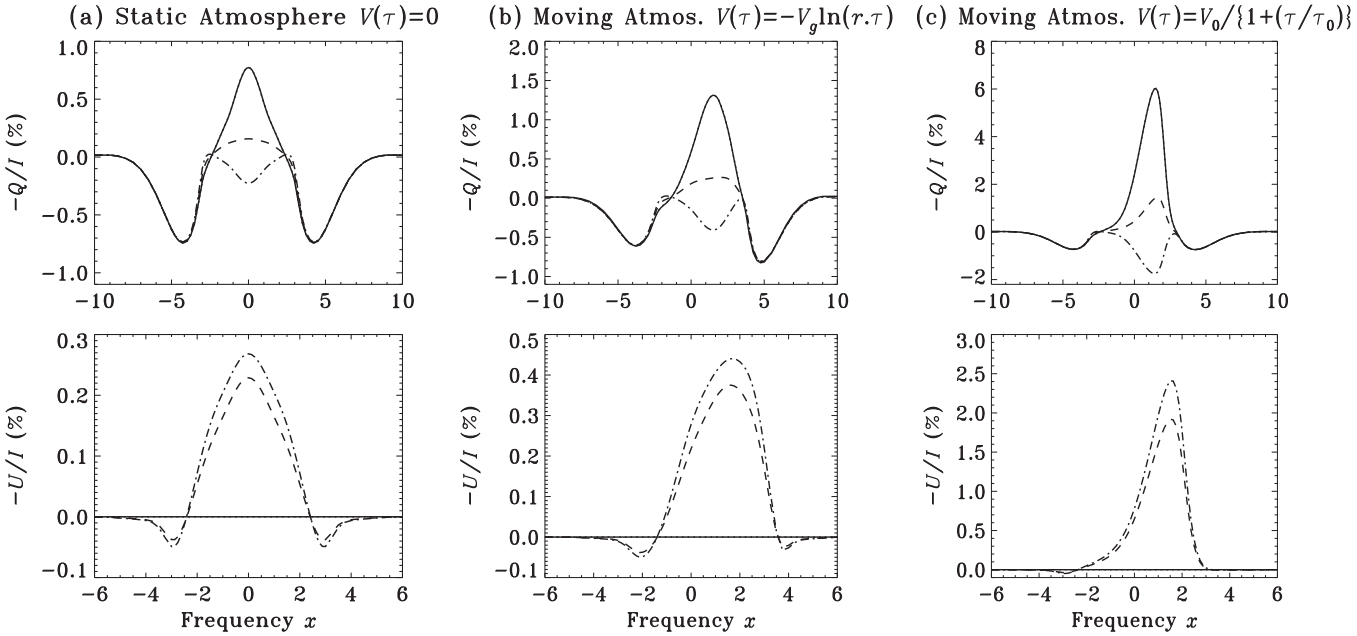

Figure 17. Comparison of non-magnetic (solid lines) and magnetic Q/I and U/I profiles for a static atmosphere (panel (a)) and for atmospheres with velocity gradients (panels (b) and (c)). The line of sight is at $\mu = 0.7$. Angle-averaged PRD is used. Other model parameters are the same as in Figure 13. Different line types are: dotted ($\theta_B = 0°$), dashed ($\theta_B = 30°$), and dotted-dashed ($\theta_B = 90°$). Other magnetic field parameters are $\Gamma_B = 1$ and $\chi_B = 0°$.

In this paper we have studied the effect of vertical velocity fields on the polarization profiles of optically thick lines both in the presence and in the absence of magnetic fields. As in previous studies (see Carlin et al. 2012, also Sampoorna & Nagendra 2015 where only optically thin lines were considered), we find that, when compared to the static or constantly moving atmospheres, the presence of vertical velocity gradients in the medium enhances the linear polarization and produces Doppler-shifted line profiles that are asymmetric about the line center. More importantly the presence of velocity fields in those layers of the atmosphere where the line wings are formed gives rise to asymmetric PRD wing peaks and also asymmetry in the minima between the core peak and PRD wing peaks. For the linear velocity law considered in this paper, the asymmetry in the core minima is clearly visible, while that in PRD wing peaks is marginally seen. We remark that a spatially confined, shock-like increase in velocity in the regions where the PRD wing peaks are formed can lead to larger asymmetry in the PRD wing peaks. The comoving frame method developed in this paper can handle only monotonic velocity fields. In a forthcoming paper we will extend this method to treat non-monotonic velocity fields, the inclusion of which would require considerable changes in the formal solution (see BH04 for more details).

Our numerical studies show that, like in the static case, even in the case of moving atmospheres, the angle-dependent PRD effects for an optically thick line are important only in the computation of the U/I profiles, which are generated when a weak magnetic field is present in the medium. For the computation of the I and Q/I profiles of optically thick lines one can safely assume angle-averaged PRD irrespective of whether the atmosphere is moving or static. Finally we stress that for a correct diagnostic of the weak magnetic field via the Hanle effect, it is necessary to take into account the effects of velocity fields when computing the linear polarization profiles.

The authors are grateful to an anonymous referee for constructive comments that helped to substantially improve the paper. Computations are performed on a 20 node HYDRA cluster (dual Xeon X5675 with 6 cores per processor and 3.06 GHz clock speed), FORNAX (dual Opteron 6220 with 8 cores and 3.0 GHz clock speed), and KASPAR (dual Xeon X5675 with 6 cores per processor and 3.06 GHz clock speed) computing facilities at the Indian Institute of Astrophysics.

APPENDIX
COMPUTATIONAL REQUIREMENTS

We first discuss the computational aspects of the observer's frame method (see Appendix A.1) and then those of the comoving frame method (see Appendix A.2).

A.1. Observer's Frame Method

For this method, the specifications concerning frequency, depth, and angle gridding are exactly the same as those discussed in Mihalas (1978, see also Carlin et al. 2012; Hubeny & Mihalas 2014). These specifications are over and above those concerning the use of angle-averaged or angle-dependent PRD in static media (see, e.g., Nagendra & Sampoorna 2011). To accurately take into account the effects of a velocity gradient in the computation of the optical depth increments in the formal solution, it is necessary to use a large number of depth points per decade. In other words, the depth grid should be chosen such that changes in V between successive depth points should be less than or equal to 0.5 Doppler widths. For the results presented in Sampoorna & Nagendra (2015, and also in the present paper), we have chosen 20 points per decade. Such a high resolution was chosen to demonstrate the scaling of the method in terms of accuracy and speed. For practical problems the actual resolution required is determined mainly by the steepness of the velocity gradient. For instance, for the velocity laws considered in this paper (see Section 4.1), about

Table 1
Computational Requirements of the Observer's and Comoving Frame Methods

	Observer's Frame Method		Co-moving Frame Method	
Case	Memory	CPU Time	Memory	CPU Time
AA-PRD + non-magnetic	2 GB	860 minute 53 s	50 MB	9 s
AD-PRD + non-magnetic	7.3 GB	815 minute 53 s	97 MB	10 minute 25 s
AA-PRD + magnetic	42.8 GB	2638 minute 28 s	306 MB	3 minute 21 s
AD-PRD + magnetic	90.6 GB	2238 minute 39 s	1.8 GB	116 minute 34 s

Note. The model values used for the computations are: $T = 100$, $r = 10^{-8}$, $\epsilon = 10^{-6}$, $a = 10^{-3}$ with 81 depth points, 73 frequency points (for the frequency range $[-12, +12]$), and 5 angle points. The convergence criterion of 10^{-4} is used. The velocity law given by Equation (26) is used with $V_0 = 3$ and $\tau_0 = 1$. The computations are performed on a dual Xeon X5675 with six cores per processor and 3.06 GHz clock speed.

eight points per decade is sufficient. Thus the requirement of large frequency bandwidths (needed in the presence of velocity fields), and of fine angle and depth grids, results in a severe demand on both the computing and memory resources.

In Table 1, we present the computational requirements of the observer's frame method both in the presence and in the absence of a magnetic field and for angle-averaged and angle-dependent PRD cases. For the non-magnetic case, the number of real irreducible components reduces to two for angle-averaged PRD and to four for angle-dependent PRD (see Frisch 2010; Sampoorna et al. 2011). In the presence of a magnetic field, the number of real irreducible components is six for angle-averaged PRD and 2×54 for angle-dependent PRD (see Nagendra & Sampoorna 2011). We recall that in the presence of depth-dependent velocity fields, the redistribution functions and the PRD matrix $\boldsymbol{N}^r$ in the observer's frame become depth-dependent although an isothermal model atmosphere is assumed. The quantities that require a significant amount of memory are the redistribution functions, PRD matrix $\boldsymbol{N}^r$, and the matrices $\boldsymbol{A}$ and $\boldsymbol{\mathcal{A}}$ (see Equations (12) and (13)) of the numerical method used to solve the observer's frame polarized transfer equation (see Section 3.1). This explains the large difference in memory and CPU time between the non-magnetic and magnetic cases.

We now discuss the differences in memory requirement for angle-average PRD and angle-dependent PRD. In the non-magnetic angle-averaged PRD case, only one type II redistribution function (which is now dependent on angle, frequency and depth) has to be computed and stored, whereas in the corresponding angle-dependent PRD case three azimuthal Fourier coefficients of order 0–2 for the type II redistribution function need to be computed and stored (Frisch 2010; Sampoorna et al. 2011). We remark that in the presence of elastic collisions one type III function for the angle-averaged PRD case and three azimuthal Fourier coefficients of type III for the angle-dependent case have to be computed and stored. Furthermore, the dimensionality of matrix $\boldsymbol{\mathcal{A}}$ for the angle-averaged PRD case is $(2N_x\ 2N_\mu \times 2N_x\ 2N_\mu)$, while it is $(4N_x\ 2N_\mu \times 4N_x\ 2N_\mu)$ for the angle-dependent PRD case. This explains the difference in memory requirement between the angle-averaged and angle-dependent PRD for the non-magnetic case. In the magnetic case, the requirement of significantly more memory for the angle-dependent case than the angle-averaged case comes from the fact that in the angle-dependent case an azimuthal Fourier expansion of the redistribution functions (see Frisch 2009, or Nagendra & Sampoorna 2011) results in complex irreducible Fourier components of order k (see Equation (8)), which takes values $0, \pm1, \pm2, \pm3, \pm4$. Also, since Approximation I of Bommier (1997) is used for the exact Hanle PRD matrix, the number of magnetic redistribution functions of type II to be computed to assemble the grand $\boldsymbol{N}^r$ matrix is 6 for the angle-averaged PRD case and 30 for the angle-dependent PRD case (due to azimuthal Fourier expansion).

A.2. Co-moving Frame Method

The computational requirements of the comoving frame method are similar to those for the static media case. Therefore we do not elaborate on the grid construction strategies. The only point to note is the requirement of finer depth, frequency, and angle grids in the second step (see Section 3.2) where one transforms from the comoving frame solution to the observer's frame. However, this does not add to the computational overheads because it involves only one extra formal solution in the observer's frame. For comparison, in Table 1 (rightmost column) we give the computational requirements of the comoving frame method, for the same model parameters as those used for observer's frame method (see middle column of Table 1). Clearly, the comoving frame method requires considerably less main memory, because unlike the observer's frame method, the redistribution functions, and the PRD matrix $\boldsymbol{N}^r$ in comoving frame do not depend on the optical depth even in the presence of depth-dependent velocity fields. Also, for the non-magnetic case the line source vector corrections in the comoving frame method can be computed using a core–wing technique (Paletou & Auer 1995; Nagendra et al. 1999; Sampoorna et al. 2011), unlike in the observer's frame method where the frequency-angle by frequency-angle technique had to be adopted. In the magnetic case, due to the use of Approximation I of Bommier (1997) for the Hanle PRD matrix, the frequency by frequency approach for the angle-averaged PRD is used (Sampoorna et al. 2008), while SEM is used for the angle-dependent PRD (Nagendra & Sampoorna 2011). Further, the CPU time requirements are significantly less for the comoving frame method than for the corresponding observer's frame method. Therefore it is advantageous to use the comoving frame method, especially in the computation of optically thick line profiles in high-velocity winds.

REFERENCES

Anusha, L. S., Nagendra, K. N., Stenflo, J. O., et al. 2010, ApJ, 718, 988
Asensio Ramos, A., & Trujillo Bueno, J. 2006, in EAS Publication Ser. 18, Radiative Transfer and Applications to Very Large Telescopes, ed. P. Stee (Les Ulis: EDP Sciences), 25
Baron, E., & Hauschildt, P. H. 2004, A&A, 427, 987 (BH04)
Bommier, V. 1997, A&A, 328, 726

Cannon, C. J. 1973, ApJ, 185, 621
Carlin, E. S., & Asensio Ramos, A. 2015, ApJ, 801, 16
Carlin, E. S., Asensio Ramos, A., & Trujillo Bueno, J. 2013, ApJ, 764, 40
Carlin, E. S., Manso Sainz, R., Asensio Ramos, A., & Trujillo Bueno, J. 2012, ApJ, 751, 5
Frisch, H. 2007, A&A, 476, 665
Frisch, H. 2009, in ASP Conf. Ser. 405, Solar Polarization 5: In Honor of Jan Stenflo, ed. S. V. Berdyugina, K. N. Nagendra & R. Ramelli (San Francisco, CA: ASP), 87
Frisch, H. 2010, A&A, 522, A41
Gandorfer, A. 2002, The Second Solar Spectrum, Vol 2 (Zurich: VdF)
Hillier, D. J. 1994, A&A, 289, 492
Hillier, D. J. 1996, A&A, 308, 521
Hubeny, I. 2003, in ASP Conf. Ser. 288, Stellar Atmosphere Modeling, ed. I. Hubeny, D. Mihalas & K. Werner (San Francisco, CA: ASP), 17
Hubeny, I., & Mihalas, D. 2014, Theory of Stellar Atmospheres: An Introduction to Astrophysical Non-equilibrium Quantitative Spectroscopic Analysis (Princeton, NJ: Princeton Univ. Press)
Landi Degl'Innocenti, E., & Landolfi, M. 2004, Polarization in Spectral Lines (Dordrecht: Kluwer)
Mihalas, D. 1978, Stellar Atmosphere (2nd ed.; San Francisco: Freeman)
Milić, I., & Faurobert, M. 2014, A&A, 571, A79
Nagendra, K. N. 1996, SoPh, 164, 67
Nagendra, K. N. 2014, in ASP Conf. Ser. 489, Solar Polarization 7, ed. K. N. Nagendra et al. (San Francisco, CA: ASP), 179
Nagendra, K. N., Frisch, H., & Faurobert-Scholl, M. 1998, A&A, 332, 610
Nagendra, K. N., Paletou, F., Frisch, H., & Faurobert-Scholl, M. 1999, in ASSL 243, Solar Polarization, ed. K. N. Nagendra & J. O. Stenflo (Boston: Kluwer), 127
Nagendra, K. N., & Sampoorna, M. 2011, A&A, 535, A88
Nagendra, K. N., & Sampoorna, M. 2009, in ASP Conf. Ser. 405, Solar Polarization 5: In Honor of Jan Stenflo, ed. S. V. Berdyugina, K. N. Nagendra & R. Ramelli (San Francisco, CA: ASP), 261
Olson, G. L., & Kunasz, P. B. 1987, JQSRT, 38, 325
Paletou, F., & Auer, L. H. 1995, A&A, 297, 771
Sampoorna, M. 2014, in ASP Conf. Ser. 489, Solar Polarization 7, ed. K. N. Nagendra et al. (San Francisco, CA: ASP), 197
Sampoorna, M., & Nagendra, K. N. 2015, in IAUS 305, Polarimetry: From the Sun to Stars and Stellar Environments, ed. K. N. Nagendra et al. (Cambridge: CUP), 387
Sampoorna, M., Nagendra, K. N., & Frisch, H. 2008, JQSRT, 109, 2349
Sampoorna, M., Nagendra, K. N., & Frisch, H. 2011, A&A, 527, A89
Sengupta, S. 1993, MNRAS, 265, 513
Stenflo, J. O. 1994, Solar Magnetic Fields—Polarized Radiation Diagnostics (Dordrecht: Kluwer)
Supriya, H. D., Smitha, H. N., Nagendra, K. N., et al. 2014, ApJ, 793, 42